REVIEW ARTICLE

Check for updates

Advanced spectroscopic techniques for characterizing defects in perovskite solar cells

Saurabh Srivastava [1], Sudhir Ranjan[2], Lokesh Yadav[3], Tejasvini Sharma[4], Shivani Choudhary[4], Daksh Agarwal[5], Anand Singh[3,6,7 ✉], Soumitra Satapathi[4], Raju Kumar Gupta[2,3,7,8 ✉], Ashish Garg[3,7 ✉] & Kanwar S. Nalwa[3,7 ✉]

There is currently substantial interest in commercializing perovskite solar cells as they offer superior properties over silicon-based solar cells, such as ability for bandgap tuning, higher absorption coefficients, and potentially lower manufacturing costs. However, trap states originating from ionic vacancies, imperfect interfaces, and grain boundaries have hampered their performance and long-term stability during operation. Identifying and quantifying defects in perovskite solar cells becomes inevitable to address these challenges and mitigate the deteriorating effects of these defects. This Review focuses on recent developments in optical and electrical characterization techniques employed for the investigation of defects in halide perovskites and the techniques to understand ion migration in devices. We focus on sample preparation, advantages, limitations, and the nature of information obtained from each of the spectroscopic techniques. This Review will enable the researchers to understand and identify suitable characterization techniques for characterizing defect concentrations and their energetic and spatial distribution in perovskite solar cells.

The development and study of perovskite solar cells is a contemporary area due to their favorable characteristics such as tunable bandgap, high absorption coefficient, low exciton binding energy, balanced and long-range ambipolar transport properties, and high charge carrier mobilities[1–3]. These excellent optoelectronic properties have enabled perovskite solar cells (PSCs) to achieve remarkably high-power conversion efficiencies (PCE) of 25.7% within a span of ten years since they were first demonstrated in 2009 with a PCE of 3.8%[4,5]. Ease of solution processing, simple film fabrication steps, and soft nature of perovskite thin films offer promise for large-scale PSC module development for commercialization in the near future[6]. Despite these advantages, the soft structure of halide perovskite results in a significant level of unintentional defects that hamper its optoelectronic properties, thereby adversely affecting the PCE and long-term ambient stability of the PSCs[7]. These defects originate mainly from the disorder in the structure of the perovskite crystals and significantly modulate the energy levels and their spatial distributions, critically impacting the photophysical properties of the perovskites[8]. The reported PCE of the PSCs is still lower than the Shockley–Queisser thermodynamic (SQ) limit of 31% for single-junction devices, which is attributed mostly to the shallow and deep-level defects formed during the perovskite film crystallization. These defects lead to hysteresis, nonradiative

[1] Department of Materials Science and Engineering, Indian Institute of Technology Kanpur, Kanpur 208016 U.P., India. [2] Department of Chemical Engineering, Indian Institute of Technology Kanpur, Kanpur 208016 U.P., India. [3] Department of Sustainable Energy Engineering, Indian Institute of Technology Kanpur, Kanpur 208016 U.P., India. [4] Department of Physics, Indian Institute of Technology Roorkee, Roorkee 247667 Uttarakhand, India. [5] LAM Research Corporation, Fremont, CA 94538, USA. [6] Department of Chemistry, Indian Institute of Technology Kanpur, Kanpur 208016 U.P., India. [7] Chandrakanta Kesavan Centre for Energy Policy and Climatic Solutions, Indian Institute of Technology Kanpur, Kanpur 208016 U.P., India. [8] Centre for Environmental Science and Engineering, Indian Institute of Technology Kanpur, Kanpur 208016 U.P., India. ✉email: anands@iitk.ac.in; guptark@iitk.ac.in; ashishg@iitk.ac.in; ksnalwa@iitk.ac.in

recombination, charge trapping-detrapping, and ion migration in perovskite thin films, thus leading to poor photovoltaic performance and ambient stability in PSCs[9–12]. The low energy of the formation of ionic defects in halide perovskites leads to the formation of ionic vacancies and hence contributes to ion migration. Ion migration, in turn, causes the screening of the effective electric field inside the perovskite layer, leading to inefficient charge carrier extraction and hence hysteresis and degradation in the devices[13,14]. Hence, it is vital to understand and characterize these defects and appropriately find ways to mitigate them. Moreover, charge carrier dynamics is a key factor that influences the efficiency and stability of devices. The trap levels within the bandgap of the semiconductors, introduced due to the defects, act as Shockley-Read-Hall (SRH) nonradiative recombination centers for the carriers, thereby negatively impacting the charge carrier dynamics[14]. Defects in PSCs emanate mainly from the external and intrinsic factors that lead to their degradation[15–17]. The intrinsic factors correspond to the intrinsic structural and chemical instability of perovskite material and its interfaces with the transport layers. On the other hand, the external factors are moisture, heat, light, and oxygen, which affect the stability of the PSCs[18–20]. Upon exposure to moisture, water molecules form strong hydrogen bonds with organic cations of perovskite, resulting in the distortion of the perovskite crystal structure, which results in faster deprotonation of the organic cation and, ultimately, degradation of the PSCs[21]. An intrinsically high concentration of iodide vacancies in perovskite promotes the adsorption of atmospheric oxygen and its diffusion in both bulk and at the surface of the crystallites. Adsorption of molecular oxygen at the vacant sites results in electron trapping, which forms highly reactive and charged superoxide O_2^-. This phenomenon results in deprotonated A-site gas, the creation of water, and PbI_2[22]. Furthermore, illumination causes photo-induced ion migration, which results in the creation of charge-trapping domains and compositional changes in the PSCs, thereby leading to structural instability of perovskites and device degradation[23]. Further, the literature shows that the perovskite films degrade under thermal stress through volatilization of organic cation and halide species, primarily in methylammonium-based perovskites[24,25]. The stable formation energy values of a $MAPbI_3$ perovskite structure typically range from 0.1–0.3 eV[26,27] (0.11–0.14 eV as per DFT calculations[24]). Remarkably, these values correspond well to the average estimated thermal energy for solar cell operation at 85 °C (0.093 eV). Consequently, when the perovskite solar cells are annealed to such temperatures, the individual unit cells can become unstable, leading to their decomposition over time. The thermal degradation occurs predominantly on the surface, then proceeds to the bulk of the perovskite and affects the interface between the perovskite and the charge transport layers, thus giving rise to a large number of defects[28]. Since, degradation pathways of PSCs are mediated by the formation of defects, developing a deeper understanding of the defect formation mechanisms during degradation is essential, which can be made possible by the use or development of appropriate defect characterization techniques and will be vital to improving the ambient performance and atmospheric robustness of the PSCs. Moreover, investigating the nature of defects, the spatial and energetic distribution of traps, and the consequent impact of defects on charge carrier dynamics and ion migration by utilizing suitable characterization tools would enable us to achieve higher carrier lifetimes, limit carrier recombination, and mitigate perovskite degradation, which are the pathways to achieving highly efficient and stable devices.

Characterization techniques that have been used to study defects are broadly classified into three categories: optical, electrical, and ion migration techniques. Optical techniques employ a pump to first excite the carriers, followed by a probe to study their interactions as they relax. Electrical techniques measure the current density or capacitance as a function of voltage or frequency, that can be used to measure the defect density and their spatial and energetic distribution. The ion migration techniques employ either applying an electric field or optical excitation or a combination of both electric field and optical excitation to investigate the spatial and temporal dynamics of ion migration at the interfaces, grain boundaries, and bulk. Figure 1 schematically exhibits the different categories of defect characterization techniques for PSCs.

This review chronicles the recent developments in the characterization techniques used to investigate the defects in the halide perovskites and their efficacy in understanding the charge carrier dynamics and ion migration. It begins with an overview of the origin of defects, and their types in the halide perovskite, followed by a discussion on the impact of these defects on the performance of PSCs. Further, the review critically assesses the optical and electrical defect characterization methods, including techniques used to investigate ion migration in PSCs. Finally, an outlook and perspective are provided into implementing these defect characterization techniques, accurately investigating defect properties in PSCs, and developing new techniques that can help improve the stability of PSCs, leading to faster commercialization.

Defects in metal halide perovskites

Defects in crystalline semiconductors are broadly classified as crystallographic defects and impurities in the crystal lattice. Crystallographic defects can be either point defects, such as ionic vacancies, interstitials, and antisite substitutions, or higher-dimensional defects, such as grain boundaries, dislocations, and precipitates. Crystallographic defects are generated in the crystal structure during crystal growth and/or the post-treatment process. Point defects are thermodynamically stable defects, and their formation energy depends on the atomic bond energies as well as thermodynamic parameters such as enthalpy and entropy of the reaction, while their concentration strongly depends on the processing conditions such as temperature. Defects in semiconductors are often considered detrimental as they adversely impact semiconductor properties such as charge carrier mobility, conductivity, and carrier lifetimes[29].

Charge recombination centers, also known as trap states, are formed within the bandgap of semiconductors due to point defects in the crystals. These trap states can exist as either shallow or deep electron traps, and their specific positions are determined by the energy levels in relation to the valence band maximum and/or conduction band minimum. The extensively researched perovskite compound, methylammonium lead triiodide ($MAPbI_3$) exhibits a diverse range of intrinsic point defects, amounting to a total of 12 distinct types. These defects include vacancies (V_{MA}, V_{Pb}, and V_I), interstitials (MA_i, Pb_i, and I_i), and antisites (MA_{Pb}, MA_I, Pb_{MA}, Pb_I, I_{MA}, and I_{Pb})[26,27,30–32]. Theoretical investigations have indicated that the point defects present in $MAPbI_3$, which give rise to deep-level defects within the bandgap, possess relatively higher formation energies. Conversely, point defects with lower formation energies are associated with shallow trap states[27,30]. At room temperature, shallow point defects in the crystal structure of the material lead to unintentional doping. The defects acting as acceptors include V_{MA}, V_{Pb}, I_i, MA_{Pb}, I_{MA}, and I_{Pb}, whereas the defects functioning as donors consist of V_I, MA_i, Pb_i, Pb_{MA}, MA_I, and Pb_I[31]. Similar to the case of deep-level defects under certain growth conditions, shallow defects with low formation energies (V_{Pb}, V_{MA}, MA_{Pb}, and I_i) are acceptors, and MA_i, V_I, and MA_I, are donors[31,32]. The precise control of growth conditions allows for the intrinsic doping of
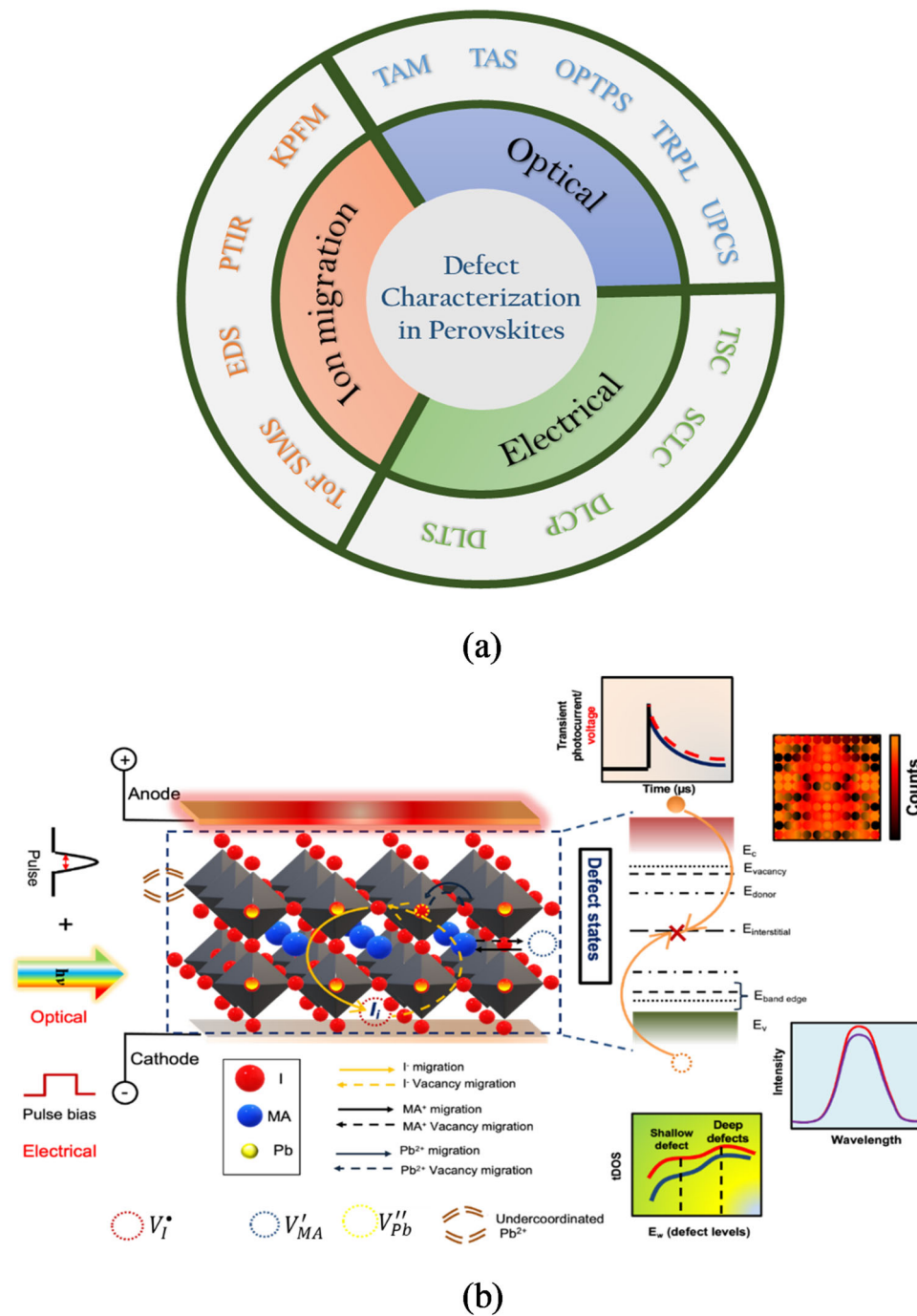
Fig. 1 Pie chart demonstrating electrical, optical, and ion migration techniques used for defect characterization in perovskite solar cells. a Various defect characterization techniques are categorized under optical, electrical, and ion migration. b Schematic summarizing the various defect characterization techniques.

MAPbI$_3$ to undergo a transition from p-type to n-type. This transition is made possible by the presence of shallow donors and acceptors with low formation energies. Further, under stoichiometric growth conditions, defect formation in halide perovskites is dominated by the Schottky defect[33].

Among higher dimensional defects, grain boundaries can act as a source of shallow traps in perovskites[34], leading to hysteresis that should be minimized. This effect of ion migration is also more dominant along the grain boundaries and interfaces than in the bulk film[35]. Furthermore, the existence of shallow electronic traps arising from ionic vacancies in perovskites carries the risk of transforming into deep traps upon interaction with moisture and oxygen. Because the absorption of water and oxygen molecules at these vacant sites is significantly more favorable than on pristine surfaces, perovskite degradation is accelerated through the vacancy-assisted decomposition mechanism[36]. Perovskite devices with fewer grain boundaries, a bigger grain size, and fewer defects in perovskite films have better performance, higher ambient stability, and lower hysteresis[37,38].

Defects within the perovskite layer have an adverse effect on carrier transport, carrier recombination, and the band alignment between perovskite and charge transport layers, which degrades device performance. Both bulk and interfacial defects play a significant role in enhancing the nonradiative recombination in the
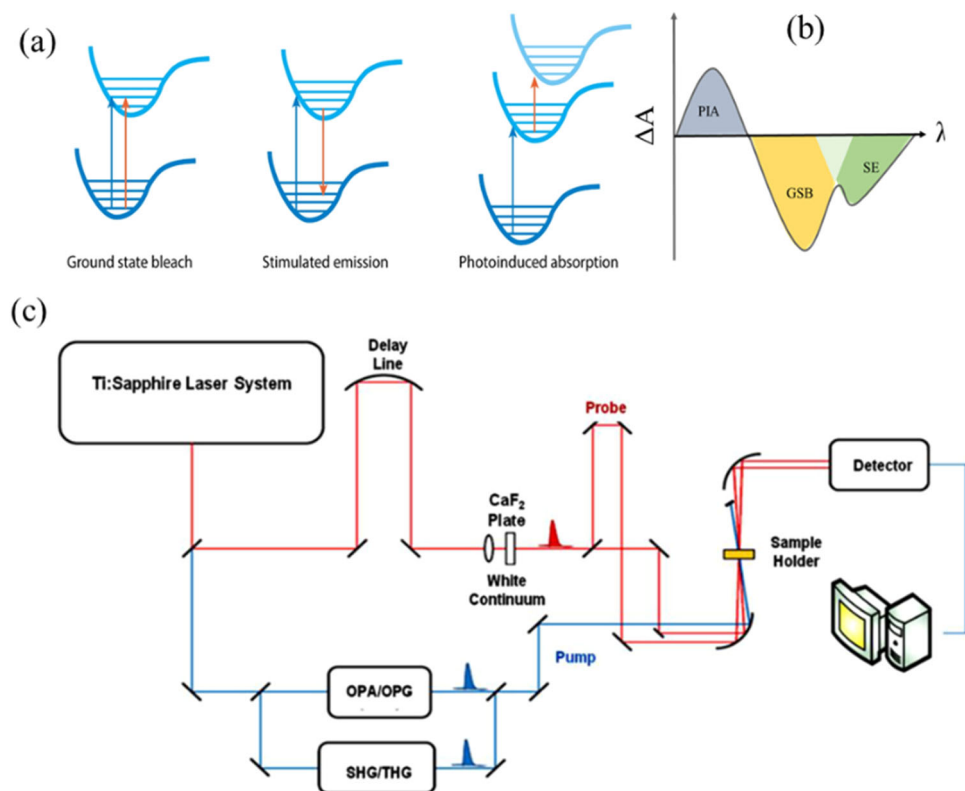
Fig. 2 Mechanistic diagram of transient absorption spectroscopy and related instrumental setup. a The energy band diagram showing the carrier excitation in TA, which results in the different bands in TA spectra (GSB, SE, and PIA). **b** Schematic illustration of typical TA spectra showing the PIA, GSB, and SE. **c** Schematic illustration of ultrafast transient absorption instrument. Reproduced with permission from ref. [40], copyright (Multidisciplinary Digital Publishing Institute, 2020).

device, and thus lowering its performance[39]. Therefore, to achieve PCE close to the theoretical maximum in PSCs, it is critical to synthesize perovskites with the lowest possible defects. This requires the ability to characterize and quantify the defects so that further improvement directions can be suggested to mitigate the formation of these defects. The improvement in PSC efficiency and stability could be achieved by optimization of processing parameters, the introduction of chemical additives, interfacial engineering, or fine-tuning the composition, but will be guided by the detailed evaluation of defects in the perovskites. In the following section, various techniques for defect characterization have been summarized along with recent results and advances.

Optical techniques

Carrier dynamics strongly affect the photovoltaic device performance of the perovskite materials, and the diffusion and transport of these carriers are extremely sensitive to the defect states present in the system. Optical techniques employ a pump to first excite the carriers, followed by a probe to study their interactions.

Transient absorption (TA) spectroscopy. TA spectroscopy is another pump-probe technique used to visualize ultrafast carrier dynamics and investigate defects and traps[40–43]. In this technique, the change in reflection $(\triangle R/R)$, absorption $(\triangle A/A)$, and transmission $(\triangle T/T)$ of a sample excited by a pump beam is measured by the time-delayed probe beam[44]. The system is stimulated by a laser pulse (pump), while the response of the excited state is monitored by a second delayed pulse (probe). Depending on the method of collecting the probe beam, changes in probe intensity $(\triangle I/I)$ induced by the pump can be quantified and

presented as $(\triangle A/A)$ (change in absorption), $(\triangle R/R)$ (change in reflection), and $(\triangle T/T)$ (transmission change). Typically, transient absorption spectra exhibit both positive and negative signals. Negative regions in a plot of $(\triangle A/A)$ versus wavelength indicate stimulated emission (SE) from an excited state and ground state bleaching (GSB), while positive $(\triangle A/A)$ values correspond to photoinduced absorption (PIA). The mechanistic diagram of how these bands appear is shown in Fig. 2[40–44].

G. Motti et al. demonstrated the defect activity in the $MAPbBr_3$ and $MAPbI_3$ perovskites thin films using TA spectroscopy. In this work, the authors have compared the band-to-band recombination dynamics to the TA dynamics for these perovskite films probed at the band edge at 525 nm for $MAPbBr_3$ film and 770 nm for $MAPbI_3$ film. A photobleach signal was observed in both films due to the state-filling by the photoexcited species. The photobleaching signal observed can be linked to the combined densities of electrons in the conduction band and holes in the valence band. Consequently, this signal enables the examination of both radiative and nonradiative recombination pathways, including trap-assisted recombination. While the trapped carriers do not directly contribute to the photobleaching, their presence can result in an imbalanced charge in the opposite band, indirectly contributing to the observed photobleaching signal. In the $MAPbBr_3$ film, the photobleaching kinetics show fast and slow lifetime components, as shown in Fig. 3a, which correspond to the band-to-band decay and the sub-band-gap emission in the IR range (trapped carrier recombination), respectively. Within the $MAPbI_3$ film, a broad emissive band with a peak around 1000 nm (1.2 eV) was observed, characterized by a relatively short lifetime lasting only a few nanoseconds. However, the photobleaching dynamics depicted in Fig. 3b indicate the existence of
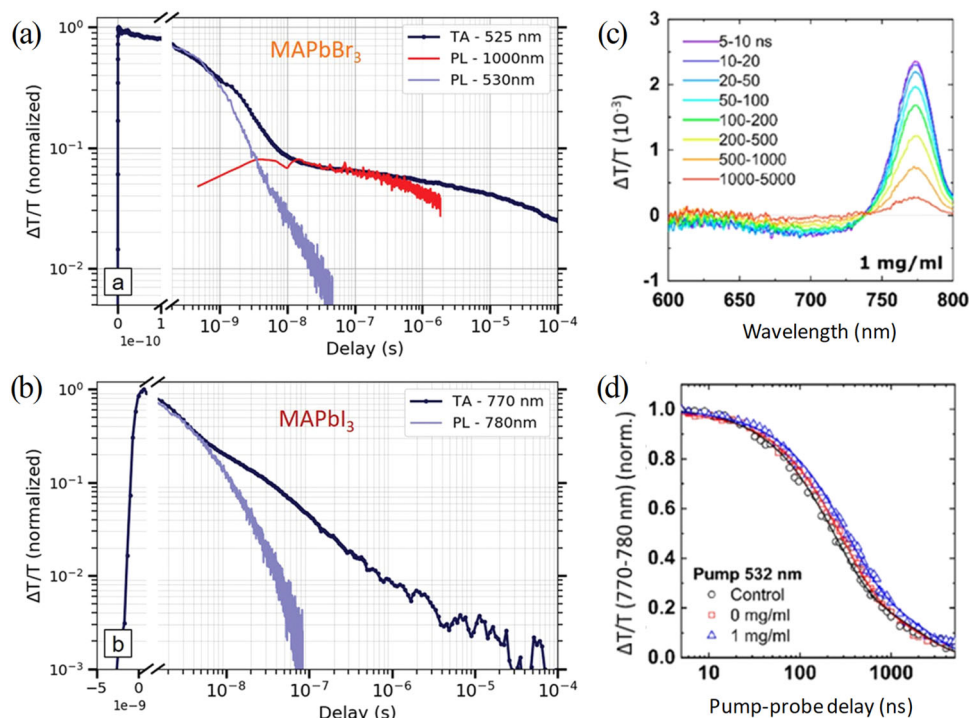
Fig. 3 Probing charge carrier dynamics using transient absorption (TA) spectroscopy. a Overlapped figure of TA dynamics of a MAPbBr$_3$ thin film probed at the band edge (525 nm, dark blue), PL dynamics at the band edge (530 nm, light blue), and 1000 nm (red). **b** TA dynamics (dark blue) of a MAPbI$_3$ thin film probed at the band edge (770 nm), overlapped with the PL dynamics at the band edge (780 nm, light blue). Reproduced with permission from ref. [45], copyright (Wiley-VCH Verlag GmbH & Co., 2019). **c** TA measurements of the sample treated with 1 mg/mL FAI (at various time delays). **d** Comparison of the decays of ground state bleach in all three studied samples. Reproduced with permission from ref. [46], copyright (American Chemical Society, 2020).

trapped carriers in MAPbI$_3$ that undergo decay on the microsecond time scale. The photobleaching dynamics observed in both MAPbBr$_3$ and MAPbI$_3$ films demonstrate the presence of trapped carriers' decay on microsecond time scales. However, these trapped carriers are either weakly emissive or deeply trapped[45]. Further, Xin et al. demonstrated the defect healing in the MAFAPbI$_{3-x}$Br$_x$ perovskites using TA spectroscopy. In this study, thin films of MAFAPbI$_{3-x}$Br$_x$ were treated with solutions of formamidinium iodide/isopropyl alcohol (FAI/IPA) at concentrations of 0 mg ml^{-1} (pure IPA) and 1 mg ml^{-1}. Three films without treatment (controlled film), treated with pure IPA (0 mg ml^{-1}), and treated with 1 mg ml^{-1} (FAI/IPA solution) were excited using a pulsed laser with a wavelength of 532 nm, operating at a pulse energy of 12 nJ and a frequency of 500 Hz. The authors observed a GSB signal at around 780 nm, shown in Fig. 3(c), which indicates the presence of free carriers due to nearly complete absorption (>99%) at 532 nm. The decay curves of the GSB signal averaged within 770 and 780 nm, were presented for all three samples in Fig. 3(d). The average lifetime was obtained as $\tau_{ave} = 1595$ ns for controlled, 1629 ns for 0 mg ml^{-1}, and 1910 ns for 1 mg ml^{-1} film. From the TA lifetime analysis, the authors observed the longest τ_{ave} in the FAI-treated sample, which indicates the defect density is significantly reduced after FAI-healing treatment[46].

Transient absorption microscopy (TAM). TAM is a technique that combines TAS with optical microscopy, enabling the visualization of recombination, spatial variations in carrier cooling, and transport with high temporal and spatial resolutions. A spatially resolved TAM technique is a powerful tool to characterize the trap state locations in photoactive perovskite layers.

TAM exhibits sensitivity to both non-emissive and emissive photoexcited species, which are predominantly populated and can be identified before they relax to the electronic ground state or populate trap states. This capability is achieved through measurements taken at short delay times. Snaider et al. performed carrier transport TAM imaging to image the spatial distribution of the sub-bandgap states in polycrystalline thin films of MAPbI$_3$ with two different grain sizes: film 1 (larger grain size >1 μm) and film 2 (smaller grain size ~200 nm)[47]. The TAM imaging for both film 1 and film 2 was performed at two different wavelengths: (i) 755 nm (bandgap wavelength) and (ii) 785 nm ((~60 meV below the bandgap), as shown in Fig. 4a (film 1) and 4b (film 2). The TAM image reveals that the presence of sub-bandgap states is more prominent at the interfaces and grain boundaries. Grain boundaries were found to have considerably higher ΔT intensities than grain interiors, indicating that sub-bandgap states are more common at the edges. At the 785 nm probe, film 2 shows a high intensity of ΔT on larger areas than film 1, suggesting a higher density of grain boundaries. Film 1 exhibited a shorter carrier lifetime at the grain boundary than the grain at the 755 nm probe wavelength, as shown in Fig. 4c. Besides, at 785 nm (probing the sub-bandgap state), film 2 exhibits slightly faster decay than film 1, as shown in Fig. 4d, likely due to increased charge recombination in film 2, which can be attributed to the smaller grain size and more defect/trap states at the grain boundaries.

The combination of TAM with PL emission microscopy works in a noninvasive and contactless mode, which can directly quantify and visualize the spatial distributions of emissive species with all electronic excitations. Additionally, the spatial location of the perovskite film's trap states can be mapped through this technique. In this manner, Simpson et al. demonstrated combined TAM with PL emission microscopy and performed
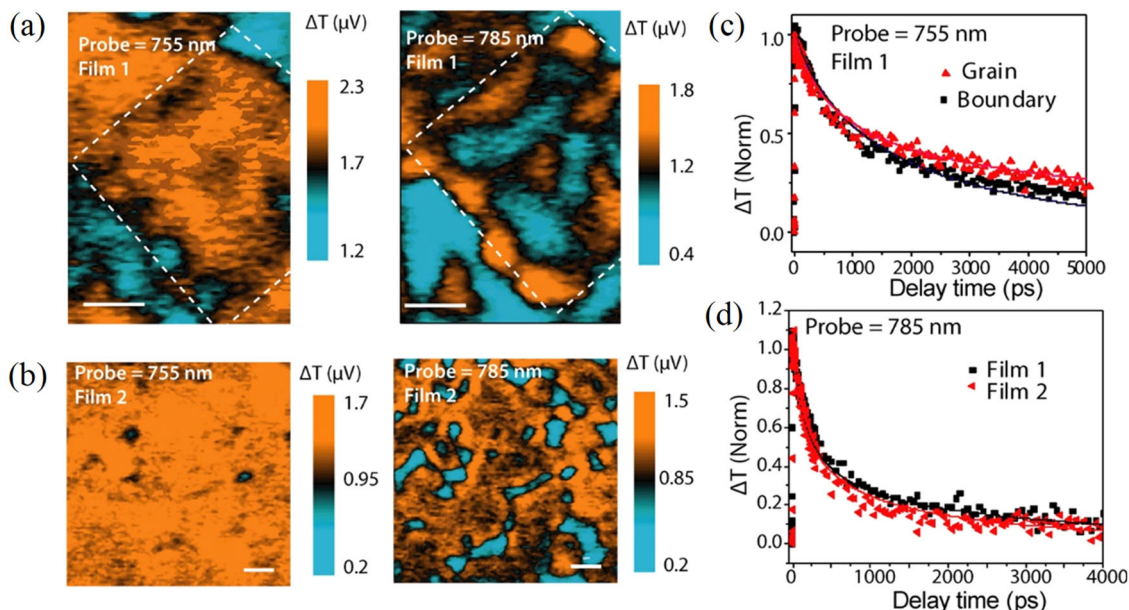
Fig. 4 Investigating charge carrier dynamics at grain boundaries and within the bulk of perovskite films using transient absorption microscopy.
Morphological TAM images of **a** MAPbI$_3$ film with a larger grain size (film 1) and **b** MAPbI$_3$ film with a smaller grain size (film 2), taken at a 10 ps time delay (pump and probe). Scale bars are 1 μm. **c** Carrier dynamics probed at 755 nm within a grain and the boundary of film 1. **d** Comparison of carrier dynamics probed at 785 nm at the boundary for film 1 and film 2. Reproduced with permission from ref. [47], copyright (American Chemical Society, 2018).
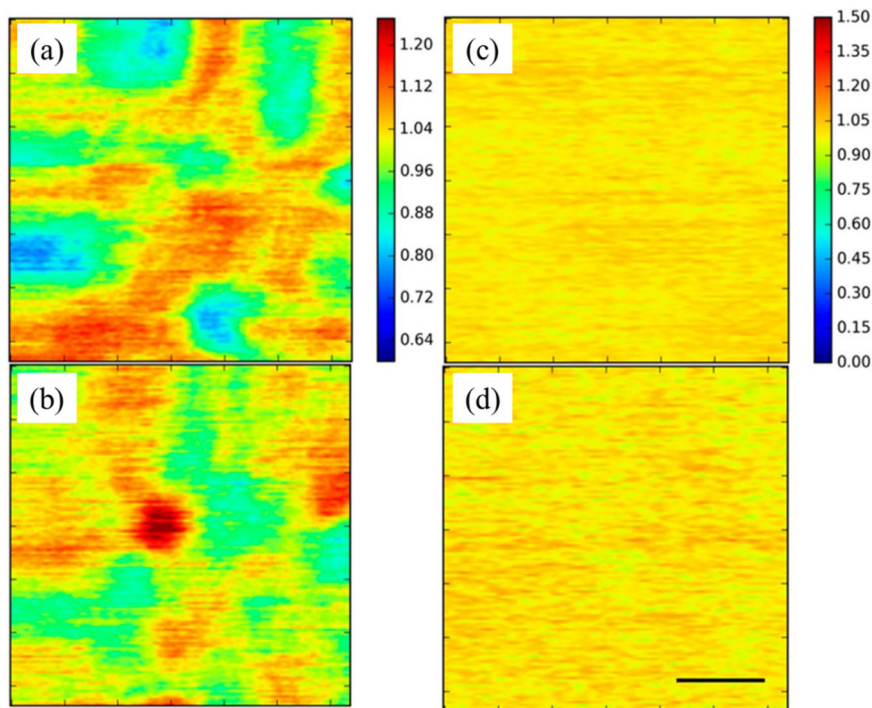

Fig. 5 Time-integrated PL mapping using transient absorption microscopy. a, b Time-integrated PL images and **c, d** femtosecond TAM images at 5 ps delay of annealed MAPbI$_3$ perovskite thin films. Images (**a**) and (**c**) are taken for 1 h annealing and images (**b**) and (**d**) are taken for 2 h annealing. The scale bar for each image is 5 μm. Reproduced with permission from ref. [48], copyright (American Chemical Society, 2016).

the spatial mapping of electronic trap states in thermally annealed MAPbI$_3$ perovskite thin films (with 1-h and 2-h annealing)[48]. In comparison to the TA amplitude, the PL intensity varies significantly at different regions, indicating the presence of traps, as shown in Fig. 5. The variation in PL intensity also implies that the electronically excited states in the perovskite film relax in a spatially dependent radiative and nonradiative manner. The

authors proposed that increasing the thermal annealing duration from 1 to 2 h can greatly minimize the spatial variability of the PL and reduce dense trapping locations by about fivefold. As a result, it can be concluded that combining PL emission microscopy with TAM is a powerful method for probing the spatial distributions of traps and defects in perovskite films by looking at the emission propensity.

Time-resolved photoluminescence (TRPL). TRPL is a technique employed to investigate the radiative recombination of charge carriers by monitoring photoluminescence[49–53]. The decay observed in TRPL is affected by a range of competitive radiative and nonradiative recombination processes taking place within the system. Consequently, TRPL can provide valuable insights into these processes and extract relevant information about them[54–57].

Yamada et al. utilized TRPL spectroscopy to examine the kinetics of photocarrier recombination in thin films of MAPbI$_3$ as a function of time since fabrication[58]. It was discovered that as the films were aged for 30 h, the PL lifetime was gradually enhanced. This was attributed to the spontaneous reduction of defects by room temperature annealing and is the major factor in the enhanced performance of aged perovskite solar cells. Wen et al. investigated the defect-trapping states and carrier recombination dynamics in MAPbI$_3$ perovskite. The study focused on perovskite samples synthesized using two different approaches: traditional spin coating and gas-assisted solution processing. The defect trapping is responsible for the fast component, which dominates the PL decay at extremely low excitations[59]. The gas-assisted sample has a longer fast component and smaller decay times than the spin-coating sample, which can be attributed to the effective defect trapping due to the larger concentration of trap states in the gas-assisted sample than the spin-coating sample. This work emphasizes the impact of the fabrication process on the trap density and, thereby, the carrier recombination dynamics.

Defect-related emission at cryogenic temperatures is a unique method to study defect states, regardless of emission mechanism. Dobrovolsky et al. explored defect-related emissions to find the relation between these emissive states and nonradiative recombination in MAPbI$_3$ films. Two different types of films were studied: pristine MAPbI$_3$ (MAPI), fabricated under ambient room conditions, and MAPbI$_3$ with a certain concentration of Cl atoms (MAPIC), fabricated in a nitrogen glovebox using commercial perovskite ink. These two films differed in terms of surface morphology and grain size (Fig. 6a, b)[60]. It was found that at the same excitation, MAPIC showed a longer PL decay lifetime and higher PL intensity than MAPI (Fig. 6c). It indicates that the MAPI film had a higher trap density, leading to more nonradiative recombination in comparison to the MAPIC film. The spatial distribution of PL at 295 and 77 K was also analyzed. When the PL of the sample at 295 K is compared with the sample

at 77 K at the same position, a defect density variation is found. An important observation is that there is no correlation between PLQY and defect emission at various places within the same sample. Contrary to that, a clear connection was found between high PLQY and a low contribution of defect emission at 77 K in two different samples, as shown in Fig. 6d. In conclusion, it indicates that the existence of local NR centers within each sample does not result in a bigger number of shallow defect states emitting at low temperatures, which means these NR centers need to have a distinct nature from shallow defect states and may even be spatially located in separate locations at the nano and microsites.

The intensity of the photoluminescence signal is directly related to the trap density, grain size, and quality of the interfaces, and these factors significantly affect the charge carrier diffusion length and other charge transport parameters. Furthermore, the photoluminescence intensity strongly depends on the crystal size of the perovskite[61]. Using super-resolution optical imaging with a spatial resolution exceeding 10 nm, Y. Tian et al. employed PL microscopy to demonstrate the light-induced photoluminescence in MAPbI$_3$, emphasizing its dependence on crystal size[62]. The PL enhancement happens on a sub-second time scale for tiny crystallites (100 nm or less), but it takes an hour for crystals of tens of microns to reach PL saturation at one sun excitation power density in the air. The authors proposed that traps are deactivated or filled by photogenerated charge carriers under light illumination, which significantly enhances the PL intensity; therefore, this phenomenon is strongly dependent on crystallite size. This concept can be useful for fabricating luminescent crystals from micron-size perovskite crystals using simple mechanical grinding.

Optical-pump terahertz-probe spectroscopy (OPTPS). Pump-probe techniques that involve femtosecond pulsed lasers and optical delay make it feasible to investigate the exciton dissociation dynamics, exciton binding energy, and free carrier generation in perovskite materials[63–65]. In OPTPS, carriers are first excited with an above bandgap excitation, followed by a THz probe to investigate the carrier dynamics. Table 1 shows the charge carrier mobility and diffusion length in different perovskites and the corresponding recombination rate constants (k_1, k_2, k_3), suggesting the type of recombination behavior dominant in these
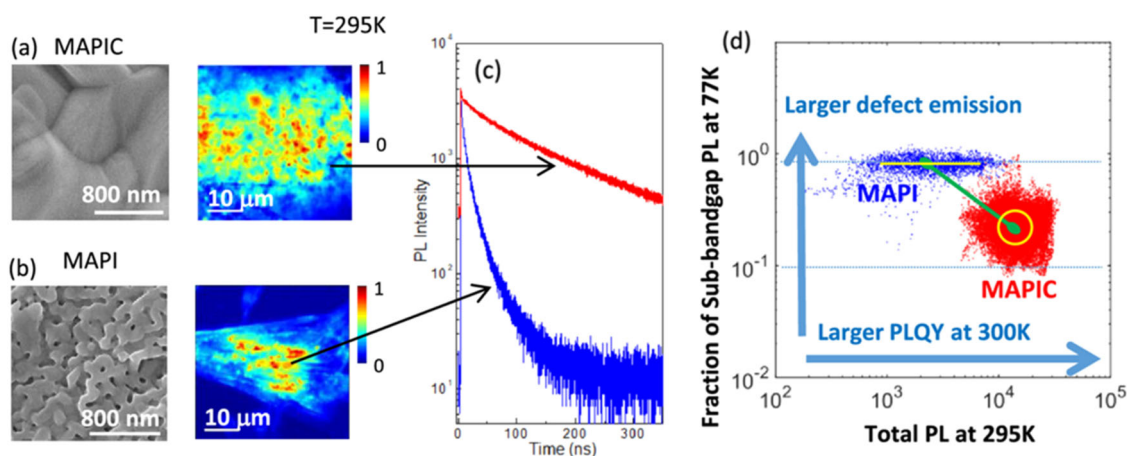

Fig. 6 Time-resolved photoluminescence decay curves of MAPI and MAPIC perovskite films. Scanning electron microscopy image and PL spectral image at 295 K for **a** MAPIC and **b** MAPI films. **c** Corresponding PL decays at 295 K. **d** Contribution of the sub-bandgap PL to the total PL at 77 K and its correlation with PL intensity at room temperature in MAPbI$_3$ perovskite film. Blue dots refer to unmodified MAPI film and red dots depict optimized MAPIC film. The correlation between the defect emission at 77 K and the PLQY of the sample is depicted in yellow. Reproduced with permission from ref. [60], copyright (American Chemical Society, 2020).

Table 1 Charge-carrier parameters and recombination rate constants for different perovskites.

Perovskite	Carrier diffusion length (μm)	Carrier mobility ($cm^2\,V^{-1}\,s^{-1}$)	Recombination rate constants			Ref.
			k_1 (s^{-1})	k_2 ($cm^3\,s^{-1}$)	k_3 ($cm^6\,s^{-1}$)	
$MAPbI_{3-x}Cl_x$	2.7	33	1.2×10^7	1.1×10^{-10}	2.3×10^{-29}	66
$FAPbI_3$	3.1	27	6.7×10^6	1.1×10^{-10}	2.2×10^{-29}	67
$FAPbBr_3$	1.3	14	21×10^6	1.1×10^{-9}	1.5×10^{-28}	67
$FAPbI_3$	25[a]	75[a]	6.7×10^6	2.97×10^{-10}	7.3×10^{-28}	119
5% KI-$Cs_{0.05}FA_{0.8}MA_{0.15}Pb(I_{0.83}Br_{0.17})_3$	-	16.2	7.9×10^6	3.2×10^{-9}	1.4×10^{-28}	120

[a]Data obtained from the fitting of the transient photoconductivity curves up to 8 ns.
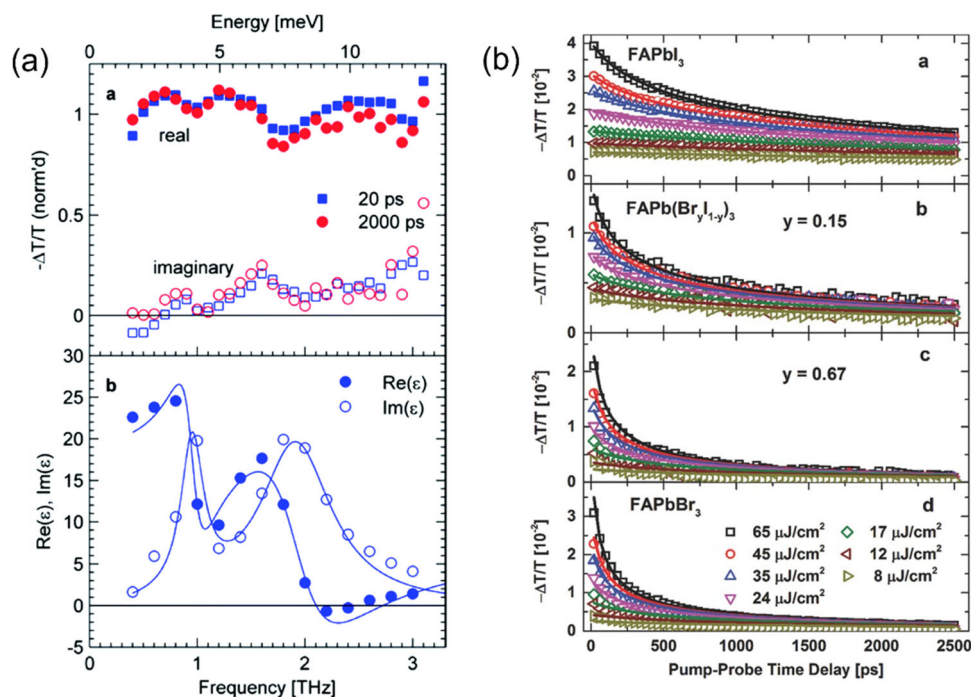

Fig. 7 Optical-pump terahertz-probe spectroscopy in $MAPbI_{3-x}Cl_x$ and $FAPb(Br_yI_{1-y})_3$ perovskite films. a Normalized THz photoinduced absorption spectra of vapor-deposited $CH_3NH_3PbI_{3-x}Cl_x$ films for time-delays 20 ps and 2 ns (excitation at 550 nm with pulse fluence 280 μJ cm^{-2}). Reproduced with permission[66]. Copyright 2014, The Royal Society of Chemistry. **b** THz photoconductivity transients of four compositions of $FAPb(Br_yI_{1-y})_3$ for excitation fluences ranging from 8 to 65 μJ cm^{-2} at 400 nm wavelength; the initial decay components of the photoconductivity transients gradually become faster on increasing the bromide content in the films. Reproduced with permission from ref. [67], copyright (Springer Nature, 2021).

perovskites. The charge carriers generated under illumination undergo different dynamic processes like carrier thermalization, carrier recombination, hot carrier relaxation, trapping, and detrapping. The charge carrier recombination kinetics are mainly governed by the availability of trap states and can be modeled by the following rate equation:

$$\frac{dn}{dt} = G - k_1 n - k_2 n^2 - k_3 n^3 \qquad (1)$$

Here k_1 represents the monomolecular charge recombination rate (typically forming immobile species by charge trapping), k_2 is the bimolecular electron-hole recombination rate constant, and k_3 the Auger recombination rate constant (the recombination of electron-hole pairs with concomitant energy transfer to a third charge). The defects or impurities within the bulk and at grain boundaries play a significant role in governing the monomolecular recombination rate, whereas the bimolecular rate constant is proportional to the charge carrier mobility, which is, in turn, affected by the defects in the system, which can impede the charge

carrier motion[66]. These rate constants can be determined from the fits of the THz photoconductivity transients obtained from the OPTPS measurements.

Wehrenfennig et al. conducted OPTPS measurements on vapor-deposited $MAPbI_{3-x}Cl_x$ films, and the recorded THz absorption spectra at pump-probe delays of 20 ps and 2 ns are shown in Fig. 7a. They obtained an enhancement in the effective charge carrier mobility (from 11 to 33 cm^2 V^{-1} s^{-1}) and diffusion length (from 2 to 2.7 μm) as compared to solution-processed films, indicating a reduction in the defect states present in the vapor-deposited perovskite films. The charge carriers exhibited a diffusion length on the scale of microns, which can be attributed to the combination of two factors: non-Langevin bimolecular electron-hole recombination and the presence of very low trap-induced monomolecular recombination pathways[66]. Similarly, Rehman et al. used OPTP spectroscopy to determine the effective charge-carrier mobilities and diffusion lengths in the $FAPb(Br_yI_{1-y})_3$ films with varying bromide content. The increase in bromide content in the perovskite films resulted in the photoconductivity transients showing faster initial decay
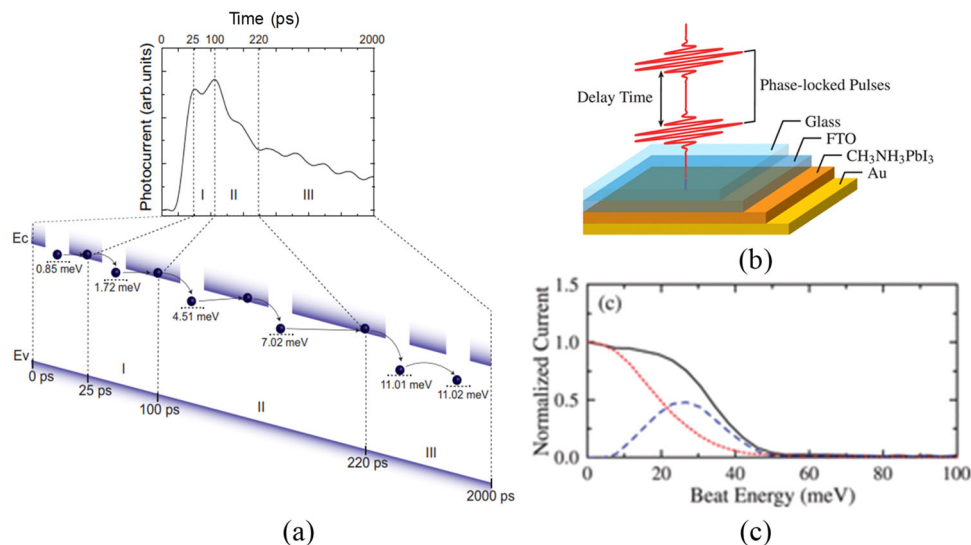
Fig. 8 Revealing trap states in MAPbI₃ perovskite films using Ultrafast photocurrent spectroscopy. a Depiction of phonon-assisted tunneling and hopping transport dynamics. Three distinct regions of the normalized photocurrent are shown under an electric field of 4×10^3 Vcm^{-1} and 20 μJ cm^{-2} laser fluence. Reproduced with permission from ref. [69], copyright (Springer Nature, 2021). **b** Schematic of sample structure and phase-locked pulse photocurrent spectroscopy. **c** Fourier transforms of photocurrent beat (solid line) and excitation pulse intensity (dotted line); the dashed line indicates the difference between these Fourier spectra. Reproduced with permission from ref. [70], copyright (American Chemical Society, 2016).

components indicative of higher-order recombination effects in the films, as shown in Fig. 7b[67]. The pure iodide-based perovskite films showed better carrier mobility and carrier diffusion length in comparison to other compositions due to the lowering of the energetic disorder in the pure iodide system, which led to fewer trap states compared to I/Br mixed phases.

Yoo et al. studied the carrier dynamics in the α-FAPbI₃ perovskite films using OPTPS and observed that the effective mobility of the perovskite films exhibited an increase when MAPbBr₃ was added in amounts ranging from 0 to 2.5 mol% (26.8–31.2 cm^2 V^{-1} s^{-1}). However, when the addition reached 10 mol%, the effective mobility decreased to 25.9 cm^2 V^{-1} s^{-1}. The improved carrier mobility of the films on MAPbBr₃ addition was attributed to the combination of increased perovskite crystal grain size and two-dimensional passivation of both grain boundaries and surface defects in the α-FAPbI₃ perovskite films[68].

Ultrafast photocurrent spectroscopy (UPCS). The ultrafast photocurrent spectroscopy technique is employed for the investigation of the ultrafast dynamics of charge carriers in photovoltaic devices by directly measuring the generated carriers as current. It is employed to examine various processes, including carrier photogeneration, transport, and recombination. This technique involves using a series of short optical pulses to initially excite the system and subsequently modulate the dynamics of the excited state. The resulting modulation effect is then observed through the photocurrent. Furthermore, this method enables the high-resolution measurement of trap states by exploiting their temperature dependence[69]. Kobbekaduwa et al. conducted a study on the dynamics of charge carrier trapping in MAPbI₃ films using the UPCS technique. They utilized temperature as a parameter to achieve extremely high-energy resolution and calculated the activation energies for the active trap states. The trap states were categorized as ultra-shallow (below 10.15 meV) and shallow (above 10.15 meV). The authors observed that the photogenerated carriers initially relaxed to the band edge within a timeframe of less than 1 ps. Subsequently, these carriers transitioned to the ultra-shallow trap states within a timeframe of less

than 25 ps, as shown in Fig. 8a. During the time range of 25 to 100 ps (region I) and 100 to 200 (region II), the carriers underwent phonon-assisted tunneling in the ultra-shallow trap states. This tunneling process involved carriers traversing the energy barrier between the ultra-shallow trap states and the conduction band. In region III, the carriers followed a hopping mechanism between the shallow trap states until they settled into slightly deeper trap states. This behavior indicated a time-independent thermal activation process[69].

Tahara et al. utilized time-domain photocurrent spectroscopy to investigate localized states near the band edge of MAPbI₃ perovskite. This technique probes localized states, including non-luminescent states, and provides a comprehensive understanding of carrier relaxation and sub-bandgap states in perovskite semiconductor thin films. To observe the ultrafast photocurrent dynamics, the authors employed a photocurrent beat spectroscopy procedure. They generated excitation pulses with a duration of 46 fs and a repetition rate of 93 MHz using a mode-locked Ti: sapphire laser. Importantly, the excitation photon energies were chosen to be significantly lower than the bandgap energy of PbI₂, thereby limiting the photocurrent signals originating from unreacted PbI₂ in the thin film samples. The excitation configuration employed for the perovskite film is shown in Fig. 8(b), where the time-domain photocurrent was measured as a function of the delay time between the two excitation pulses. By precisely controlling the relative phase between the two excitation pulses, the authors obtained constructive (in-phase) and destructive (out-of-phase) interference. Through this technique, the ultrafast photocurrent dynamics displayed a beating behavior corresponding to the resonance energy of the photocurrent generation sites. The exact position of the state energy is determined by the Fourier transform of the in-phase and out-of-phase photocurrent beating signals. The difference between these signals is shown in Fig. 8c, indicating the spectrum composed of both beating and non-beating photocurrent components when the center energy of the excitation pulse was set to 1.6 eV. The beating component of the photocurrent provides valuable insights into the generation sites of localized photocurrent, as denoted by the dashed line in Fig. 8c[70].

Differential transient transmission spectroscopy (DTTS). DTTS is a powerful technique to investigate the dynamics of charge carriers near the interface between the perovskite layer and the charge transport layers. In this method, pump-probe transmission measurements are conducted under ambient conditions using a laser as a light source, with a pulse duration of approximately 100 fs and a repetition rate of 100 kHz. The pump and probe beams are focused onto the sample surface at the same location, with respective spot sizes of 500 and 200 μm in diameter. To prevent irreversible photodegradation of the sample, the pump density is maintained at around 0.5 μJ cm^{-2}. By employing a conventional slow-scan technique, changes in the transient transmission $(\triangle T/T)$ resulting from the pump pulse are recorded at various time delays relative to the probe pulse. Ishioka et al. utilized the DTTS technique to study the injection dynamics of carriers near the perovskite and charge transport layer interface. They measured the transient transmission signals from both the perovskite side and the hole transport material (HTM) side (PTAA, PEDOT:PSS, and NiO$_x$) of the sample. For these measurements, a pump light at 400 nm and a probe light at 720 nm were employed, each with a duration of 150 fs. The pump light had a shorter optical absorption length compared to the perovskite film thickness ($\alpha^{-1} = 42$ nm), while the probe light had an absorption length exceeding the perovskite film thickness ($\alpha^{-1} = 820$ nm). The resulting transient transmission changes $(\triangle T/T)$ for the perovskite $(\triangle T_{PVK}/T)$ and the HTM $(\triangle T_{HTM}/T)$ were recorded on different time scales and are presented in Fig. 9a. Notably, the $(\triangle T_{HTM}/T)$ signals for perovskite with HTMs were consistently smaller than the $(\triangle T_{PVK}/T)$ signals for the same sample at early time delays. This observation suggests a lower hole population at the interface between MAPbI$_3$ (perovskite) and HTM compared to that at the interface with PMMA (capping layer). Over picosecond time scales, the signals from both sides exhibit complex decay and rise behaviors but ultimately converge on sub-nanosecond time scales, indicating that both sides of the perovskite films are excited at the same pump density. The differential transient transmission signal

$(\triangle T_{diff}/T \equiv \triangle T_{PVK} - \triangle T_{HTM})$ is directly proportional to the difference in the photoexcited hole populations in the perovskite for the two configurations, represented as $N_{diff}(t)$. The $(\triangle T_{diff}/T)$ signal rises and subsequently decays to nearly zero on different time scales for various HTMs, as shown in Fig. 9b.

They observed that the hole injection at the interfaces of MAPbI$_3$/PTAA and MAPbI$_3$/PEDOT: PSS occurred rapidly, within 1 and 2 ps, respectively. In contrast, hole injection at the MAPbI$_3$/NiO$_x$ interface took significantly longer, approximately 40 ps. Additionally, the devices incorporating a NiO$_x$ layer exhibited higher series resistance and lower shunt resistance, indicating suboptimal charge transfer at the perovskite interface. The presence of NiO$_x$ introduced more disorder along with defects in the perovskite film and interface, resulting in slower hole injection kinetics. Hence, the utilization of DTTS measurements can facilitate the exploration of promising HTM materials that have the potential to enhance the overall photovoltaic performance of PSCs[71].

Pump-push-probe spectroscopy (PPPS). PPPS is a transient absorption technique that involves the application of a second laser pulse, referred to as the push-pulse, temporally applied between the pump pulse and the probe pulse. The technique enables the optical manipulation of changes in excited-state carrier populations. Pollock et al. used PPPS to examine the kinetics of electron trapping in the MAPbI$_3$ perovskite system. They utilized a high-energy pump pulse to induce transitions from deep valence band electrons to trap states within the bandgap, in addition to exciting free carrier transitions. After a 10 ps delay, a NIR push-pulse was applied to stimulate the trapped electrons back to the conduction band. This temporal delay allowed the carriers induced by the pump pulse to equilibrate and establish a population of trapped electrons at the band edge, resulting in a distribution of hot carriers. The authors found that a lower-energy push-pulse (1630 nm) produced hot carrier effects but was not sufficient to excite the trapped electrons into the conduction band compared to the 1500 nm push-pulse, as
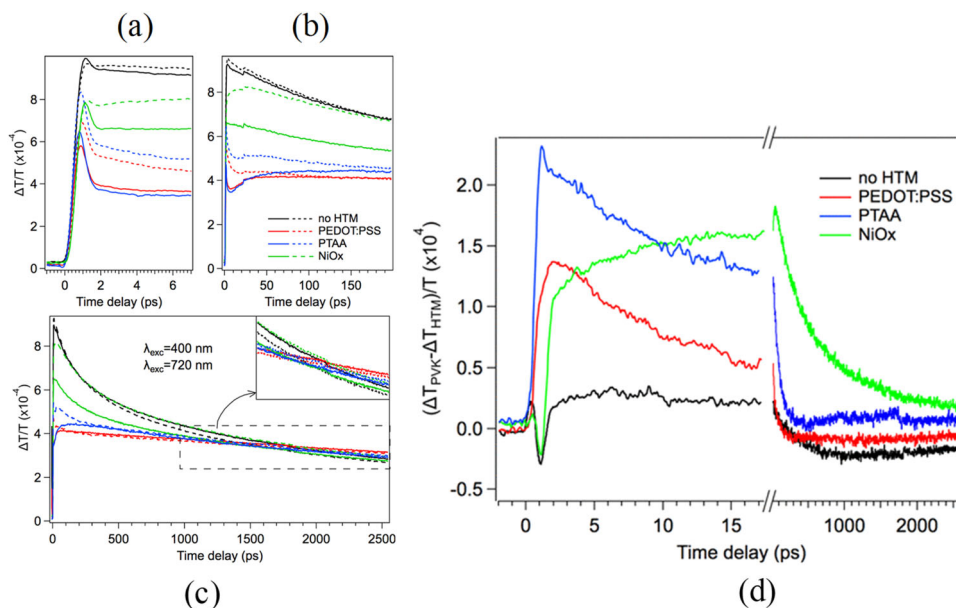

Fig. 9 Differential transient transmission spectroscopy for investigating charge carrier dynamics at perovskite/charge transport layer interface in PSC. Transient transmission changes of MAPbI$_3$ with and without different HTMs, pumped at 400 nm and probed at 720 nm on **a** picosecond, **b** sub-nanosecond, and **c** nanosecond time scales, respectively. **d** Differential transient transmission $\triangle T_{diff}/T$ of MAPbI$_3$ with and without different HTMs. Reproduced with permission from ref. [71], copyright (American Chemical Society, 2017).
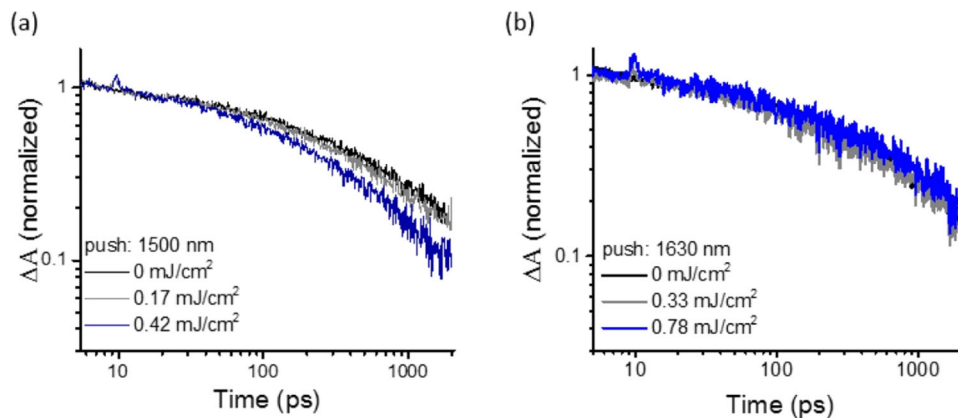
Fig. 10 Pump-push-probe spectra of MAPbI₃ perovskite films. Plot of differential absorption (ΔA) signal with respect to time delay showing the normalized pump-push-probe kinetics with **a** 1500 nm push-pulse and **b** 1630 nm push-pulse. Reproduced with permission from ref. [72], copyright (American Chemical Society, 2021).
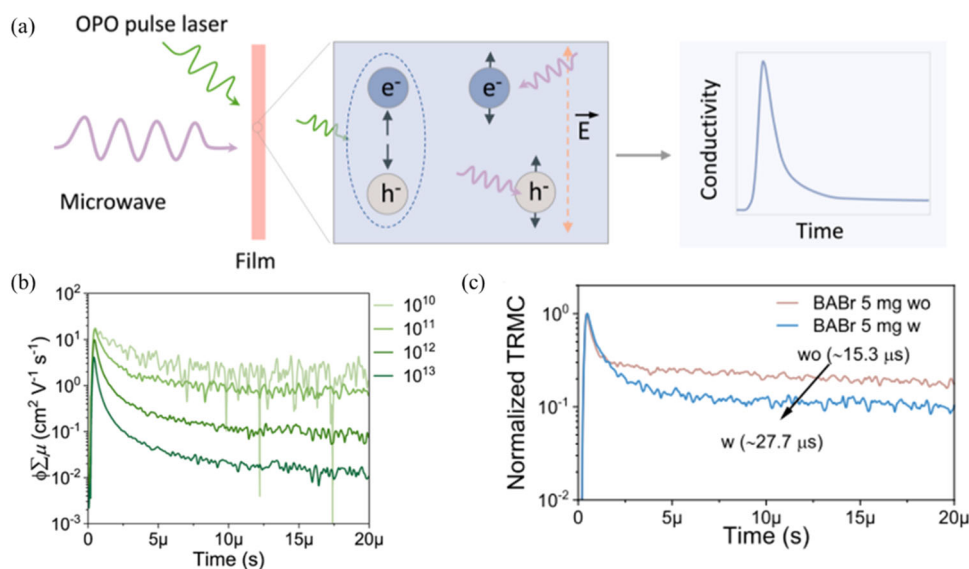

Fig. 11 Time-resolved microwave conductivity measurement in perovskite films with lower background conductivities. a Schematic illustration of the TRMC measurement. **b** TRMC transients as a function of the laser power I_0. **c** Transient ΔG vs time induced by 530 nm laser light (10^{11} photons cm^{-2}pulse^{-1}) for perovskite films with 5 mg mL^{-1} BABr with and without thermal annealing. Reproduced with permission from ref. [74], copyright (American Chemical Society, 2022).

shown in Fig. 10. This observation revealed that the energy difference between the conduction band minimum and the upper edge of the mid-gap trap state distribution in the system is ~0.83 eV[72].

Time-resolved microwave conductivity (TRMC). The TRMC technique is commonly employed to examine the dynamics of photogenerated charge carriers in semiconductor materials characterized by low background conductivities. TRMC relies on the interaction between the mobile charge carriers and the electric field component of the microwaves, allowing for the determination of photoconductivity without the influence of interfacial effects between the perovskite film and the metallic electrodes. The schematic of TRMC measurement is shown in Fig. 11a. In a typical procedure, a laser pulse is used for the photoexcitation and generation of free carriers and/or excitons in the perovskite films. The mobile free carriers in the perovskite material interact with microwaves within a cavity, leading to the absorption of energy. This interaction causes a decrease in the microwave signal, allowing for the measurement of the photoconductance (ΔG) of

the material[73]. When photoexcited charge carriers undergo recombination or become trapped in defect states, the photoconductance (ΔG) decays. By calculating the product of the charge carrier yield (ϕ) and the sum of electron and hole mobilities ($\Sigma\mu$), denoted as $\phi\Sigma\mu$, we can obtain valuable information. The change in photoconductance (ΔG) can be determined using the following equation[74,75]:

$$\phi\Sigma\mu = \frac{\Delta G}{I_0 F_A e \beta} \qquad (2)$$

Where F_A is the fraction of laser light absorbed, I_0 is the laser intensity, e is the electronic charge, and β is the ratio between the narrow and broad inner dimensions of the cavity. Yao et al. employed the TRMC method to investigate the carrier transport properties of FA$_{0.83}$Cs$_{0.17}$PbI$_{2.7}$Br$_{0.3}$ and butylammonium bromide (BABr)-treated FA$_{0.83}$Cs$_{0.17}$PbI$_{2.7}$Br$_{0.3}$ perovskite films under 530 nm laser pulse excitation at various light intensities (10^{10}–10^{13} photons cm^{-2} pulse^{-1}) as shown in Fig. 11b. In all the perovskite films, the $\phi\Sigma\mu$ decreased while ΔG decay becoming faster with increasing laser intensity. This behavior is attributed to
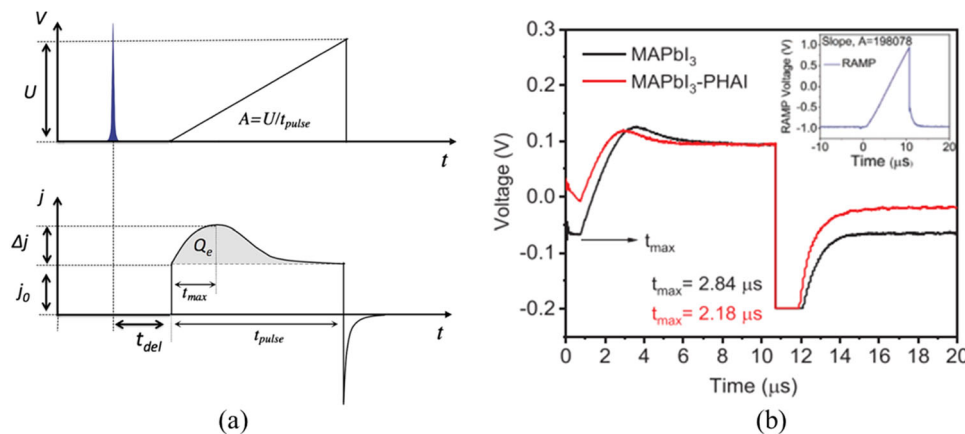
Fig. 12 Photo-CELIV measurement of MAPbI₃ perovskite films. a Illustration of the photo-CELIV technique. Triangular pulse in reverse bias after the photoexcitation of the sample (above) results in the typical CELIV transient (below) for the calculation of carrier mobility. Reproduced with permission from ref. [76], copyright (Society of Chemical Industry, 2016). **b** Photo-CELIV curves of the MAPbI₃ perovskite with and without iodide-based additive. Inset shows the slope A calculated from the ramp voltage. Reproduced with permission from ref. [77], copyright (Wiley-VCH Verlag GmbH & Co. KGaA, Weinheim, 2020).

the second-order recombination process occurring within the samples. However, the BABr-treated annealed films exhibited a slower decay of △G due to the detrapping process of the trapped carriers by the BABr-treatment. This ultimately led to an enhancement in the carrier's lifetime, as shown in Fig. 11c[74].

Photoinduced charge extraction by linearly increasing voltage (Photo-CELIV). The photo-CELIV technique is commonly used to investigate charge transport in organic semiconductors. In this measurement procedure, a voltage that increases linearly is applied to extract the photogenerated charge carriers from the perovskite film. These charge carriers have a density denoted as n and a mobility represented as μ. The perovskite film has a specific dielectric permittivity indicated by ε and a thickness denoted as d. A schematic of the technique is shown in Fig. 12a. The entire device structure can be conceptualized as a capacitor, with the perovskite film situated between two electrodes, at least one of which acts as a barrier. The transient extraction current can be determined using the following equation:

$$j(t) = j_0 + \triangle j(t) \qquad (3)$$

Where $j_0 = CA$ represents the average displacement current (C denotes the geometric capacitance and A represents the slope of the applied ramp voltage), and $\triangle j$ corresponds to the average conduction current of mobile charge carriers within the active layer. The maximum carrier extraction time (t_{max}) occurs when the films are subjected to a linearly increasing voltage with blocked contacts. Under the condition $\triangle j \leq j_0$, the charge carrier mobility can be calculated using the equation[76]:

$$\mu = \frac{2d^2}{3At_{max}^2} \qquad (4)$$

By performing photoexcitation of the perovskite films prior to the voltage sweep, the mobility estimation of the photogenerated charge carriers is obtained. Conversely, the drift mobility of equilibrium carriers is determined through measurements conducted in the dark[76]. Laskar et al. utilized the photo-CELIV technique to examine the effects of iodide-based additives on reducing the defect density in MAPbI₃ perovskite. They measured the carrier mobility and observed a significant improvement in the perovskite films with iodide additives compared to pristine films, as shown in Fig. 12b. The enhancement in carrier mobility,

as revealed by the photo-CELIV measurements, can be attributed to the passivation of defect states facilitated by the use of iodide additives[77].

Time-resolved Kerr rotation (TRKR). The TRKR technique is utilized to investigate the coherent spin dynamics of charge carriers in semiconductor materials. In a typical procedure, optical excitation is performed using a mode-locked Ti: sapphire laser with a repetition rate of 76 MHz and a pulse duration of ~1.5 ps. The laser beam is split into a circularly polarized pump beam and a linearly polarized probe beam. Both beams are then focused on the sample, resulting in a spot diameter of around 100 µm. The sample can be configured in three different geometries: Voigt geometry ($\alpha = 0°$), 53° tilted-field geometry, and 65° tilted-field geometry. Here, α represents the angle between the magnetic field **B** and the sample plane[78]. In the Voigt geometry, where magnetic fields **B** ≤ 10 T are applied, the pump pulse propagates along the z-axis, selectively exciting carriers with spins polarized along the z-direction. The subsequent coherent spin evolution, characterized by precession around the magnetic field **B**, is probed by analyzing changes in the polarization of the linear probe pulse. This allows for the examination of the coherent spin dynamics in the sample[79].

Kirstein et al. applied the TRKR technique to investigate the coherent spin dynamics of electrons and holes, as well as their interaction with the nuclear spin system, in a single crystal of MAPbI₃. Figure 13a shows the typical TRKR signal obtained from the MAPbI₃ crystal at a temperature of 7 K and a magnetic field of 0.5 T. The signal exhibits two oscillating components with distinct frequencies, which can be observed in the fast Fourier transformation (FFT) spectrum displayed in Fig. 13b. The faster precession corresponds to the electron spins with a Landè factor $g_e = +2.72$ and a spin-dephasing time $T_{2,e}^*$ of 0.4 ns, while the slower precession is associated with the hole spin with g_h of -0.56 and $T_{2,h}^*$ of 1.9 ns. The TRKR signal is attributed to resident electrons and holes generated through photogeneration, followed by their spatial separation and localization[80]. The same research group also investigated the electron and hole Landè factors in FA₀.₉Cs₀.₁PbI₂.₈Br₀.₂ perovskite crystals using the TRKR technique. They obtained $g_e = 3.57$ and $g_h = -1.21$ with long spin-dephasing times: $T_{2,e}^* = 8$ ns and $T_{2,h}^* = 5.5$ ns, respectively. The spin-dephasing times provide insights into the number of nuclear spins interacting with resident holes and electrons, as well
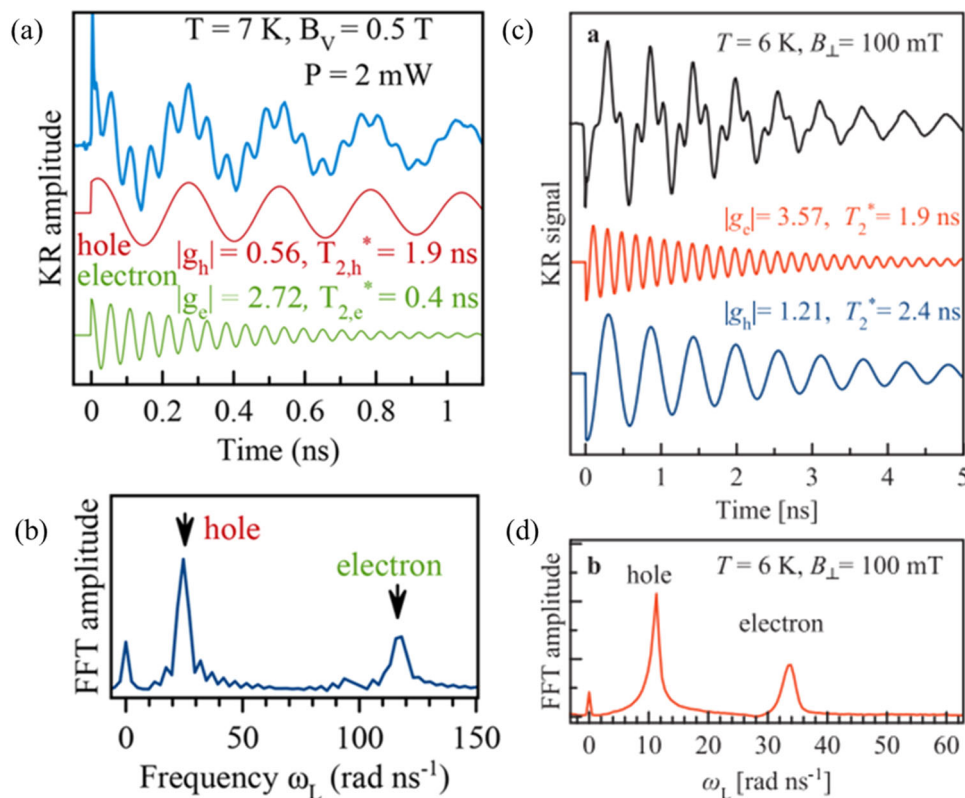
Fig. 13 Time-resolved Kerr rotation for MAPbI$_3$ perovskite system. a TRKR signal of MAPbI$_3$ crystal at a pump-power of 2 mW and **B$_v$** = 0.5 T (blue) contributed by electron (red) and hole (green) oscillating components. **b** FFT spectrum of the TRKR signal distinguishing the oscillating components in the TRKR signal. Reproduced with permission from ref. [80], copyright (American Chemical Society, 2022). **c** TRKR signal of FA$_{0.9}$Cs$_{0.1}$PbI$_{2.8}$Br$_{0.2}$ crystal at **B$_\perp$** = 100 mT (black) contributed by electron (red) and hole (blue) oscillating components. **d** FFT spectrum of the TRKR signal. Reproduced with permission from ref. [81], copyright (Wiley-VCH GmbH, 2021).

as their localization size. Figure 13c, d display the TRKR signal obtained from the FA$_{0.9}$Cs$_{0.1}$PbI$_{2.8}$Br$_{0.2}$ crystal under an applied magnetic field of 100 mT and the corresponding FFT spectrum, respectively[81].

Absolute photoluminescence quantum yield (APLQY). PLQY, or internal radiative efficiency, is a crucial parameter used to assess the intrinsic optoelectronic quality of a semiconductor film. It quantifies the ratio of radiatively emitted photons to absorbed photons, taking into account the refractive index correction. The presence of trap-mediated nonradiative recombination in the perovskite films reduces the PLQY, directly impacting the open-circuit voltage and overall conversion efficiency. The absolute PLQY can be determined by employing an integrating sphere, which collects all emissions from the sample[82,83]. Sutter-Fella et al. conducted pump-power-dependent PL measurements on MAPbI$_{3-x}$Cl$_x$ perovskite films to extract the absolute internal quantum yield (iQY). They observed that as the pump-power increased, the iQY also increased, indicating that trap states lead to low iQY levels at low optical injection levels, as shown in Fig. 14a, b. The investigation of luminescence dependence on pump-power yielded significant results. The pump-power-dependent luminescence study revealed that at a generation rate of 3×10^{22} s^{-1} cm^{-3} or higher, bimolecular recombination was the dominant process. The slope of the relationship was proportional to 1, and iQY remained constant over a range of generation rates spanning almost two orders of magnitude (observable for the sample with x = 0.1). At higher levels of optical injection, Auger recombination started to take over, causing a decrease in iQY. This led to a drop in iQY once the generation rate exceeded approximately 5×10^{24} s^{-1} cm^{-3}, equivalent to about

500 sun. In contrast, the iQY of the pure bromide sample (x = 3) was nearly 100 times lower compared to mixed halide perovskites. Furthermore, the iQY increased across the entire range of generation rates, indicating that dominant monomolecular trap-assisted recombination occurred in bromide perovskite. This indicates a higher density of traps in the pure bromide perovskite vis-a-vis the mixed halides[84].

Sub-bandgap external quantum efficiency (s-EQE). Sub-bandgap EQE or ultrasensitive EQE provides valuable insights into the sub-band states, traps, and energetic disorders, present in perovskite semiconductor devices. These sensitive EQE measurements are commonly employed to determine the energies of charge transfer states and their associated reorganization energies[85]. Cheng et al. conducted an analysis of the sub-gap region of MAPbI$_3$ perovskite solar cells by examining the evolution of the s-EQE spectra. They achieved this by calculating the difference between the EQE values after and before light soaking, denoted as Δs-EQE=s-EQE$_{soaked}$−s-EQE$_{fresh}$. Subsequently, the obtained spectra were fitted using a Gaussian model used to define the density of defect states in the perovskite material. The $\triangle$s − EQE spectra and the Gaussian fit revealed two defect states in ITO-contact devices and four defect states in Ag-contact devices, as shown in Fig. 15. The calculated defect energy level for defect state I (1.40 eV) was attributed to the vacancy and interstitial defects of V_{Pb}, V_I, I_i and MA_i, defect state II (1.22 eV) was associated with the interstitial defects of I_i and Pb_i, defect state III (1.08 eV) was linked to the vacancy and antisite of V_{Pb} and I_{Pb} and defect state IV (0.95 eV) was ascribed to the interstitial and antisite of I_i and I_{MA}. Notably, the introduction of Ag atoms/ ions
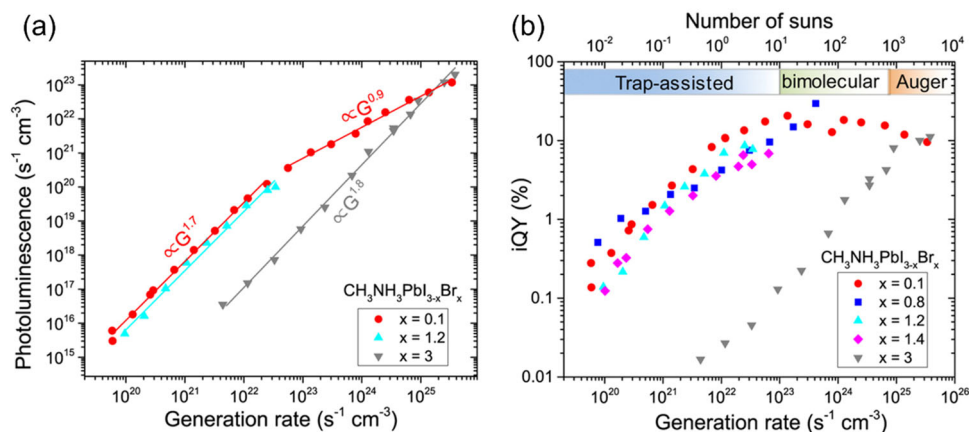
Fig. 14 Absolute photoluminescence quantum yield measurement. a Dependence of the integrated PL signal on the pump-power for samples with different bromide concentrations (x = 0.1, 1.2, and 3). **b** Pump-power dependence of the iQY. Reproduced with permission from ref. [84], copyright (American Chemical Society, 2016).
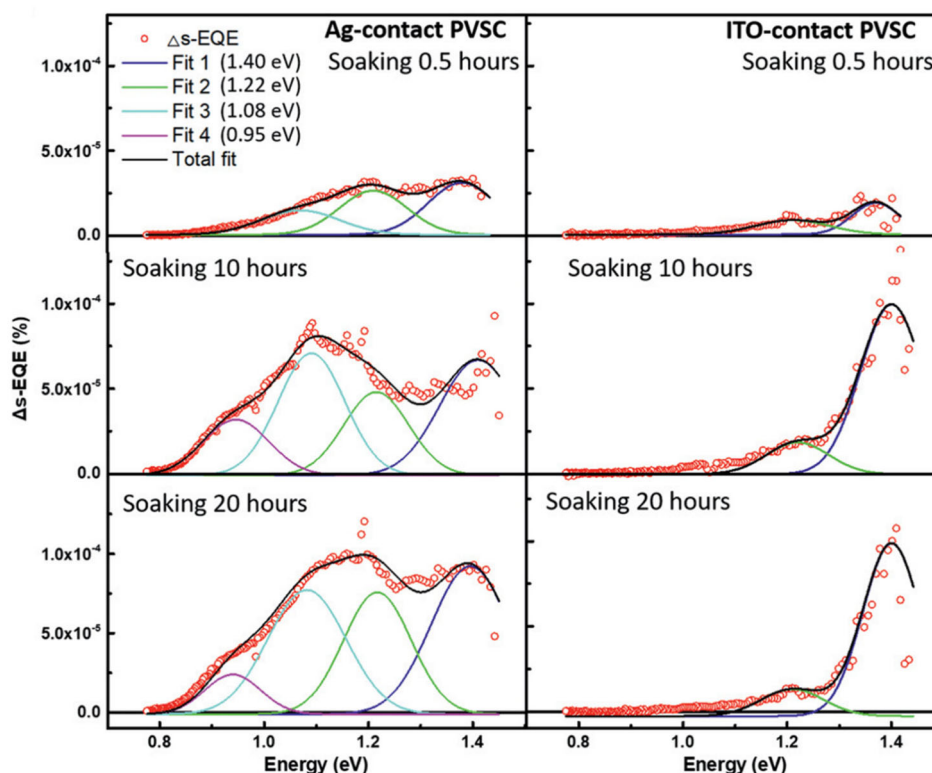

Fig. 15 Sub-bandgap external quantum efficiency measurement for determining sub-bandgap defect states in perovskite. $\triangle s - EQE$ spectra (open circle) and Gaussian fitting results (lines) of Ag-contact and ITO-contact MAPbI$_3$ devices upon light soaking (0.5, 10, and 20 h). Reproduced with permission from ref. [86], copyright (Wiley-VCH GmbH, 2021).

into the perovskite lattice was observed to induce diffusion and create defects that ultimately impact the s-EQE signal[86].

Electrical methods

Electrical methods are primarily used to characterize the spatial and energetic distribution of defects, the nature of defects, as well as defect activation energy (shallow or deep). The identification of defect passivation strategies is crucial for effectively mitigating the detrimental impact of defects on the perovskite device's performance. These techniques play a pivotal role in this process by enabling defect detection and understanding, allowing for the

development of effective strategies to suppress their negative effects.

Space-charge limited current (SCLC). The SCLC method is a commonly used defect characterization technique that has been widely employed to measure the various properties of perovskite films, such as carrier concentration, carrier mobility, conductivity, and defect density[87]. In this technique, a large electric field is applied across the semiconductor through ohmic contacts, corresponding to the charge injected into the material. Injected charges are captured by trap states leading to a reduction in the density of free charges[88]. The trap density in the semiconductor is
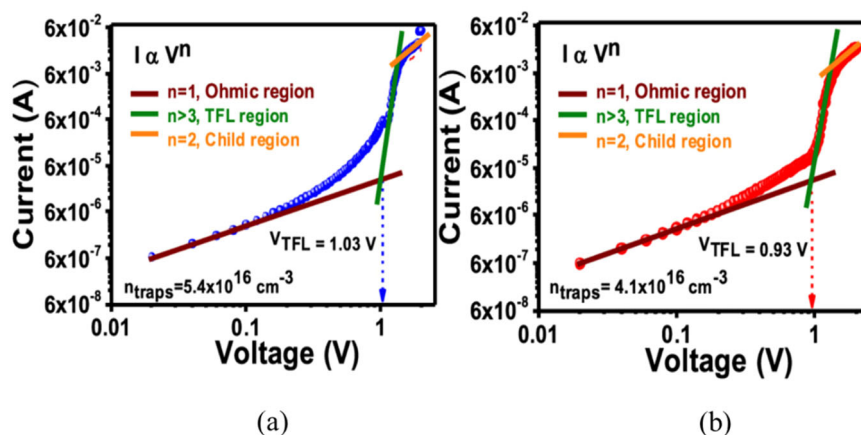
Fig. 16 Space-charge limited current measurements of MAPbI₃ perovskite devices. Typical J-V curve of an electron only **a** HT-TiO$_2$ and **b** MW-TiO$_2$ devices. Reproduced with permission from ref. [38], copyright (American Chemical Society, 2022).

calculated from the dark current vs. voltage (J-V) curve in the space-charge-injected current region. Usually, the J-V curve is divided into three different regimes depending on the voltage range: the ohmic region, the trap-filled limit (TFL) region, and the Child region. The Ohmic region is obtained at low voltages where the J-V curve is linearly fitted, and defects are filled by the injected charges. The voltage at which all the defects are filled by charges is termed trap-filled limited voltage (V_{TFL}) and at voltages above V_{TFL}, the charges are free to move through the film. This is marked by the instantaneous jump in the current to a low resistance state and can be used to calculate trap density as per Eq. 5[89]:

$$n_{traps} = \frac{2\varepsilon\varepsilon_0 V_{TFL}}{qL^2} \qquad (5)$$

where L, ε, ε_o, and q are the thickness of the film, the dielectric constant of the perovskite, the permittivity of the vacuum, and the electronic charge, respectively. Figure 16a, b shows a typical J-V curve of electron-only microwave annealed (MW)-TiO$_2$ and high temperature annealed (HT)-TiO$_2$ devices to calculate defect density[38]. It was revealed from the SCLC method that trap density in perovskite films based on MW-TiO$_2$ reduced to 4.1×10^{16} cm^{-3} compared to those in HT-TiO$_2$ (5.4×10^{16} cm^{-3}) owing to the low-temperature processing of MW-TiO$_2$, which ensures fewer defects and better interface with perovskite.

Moreover, the SCLC method can measure both the electron and hole trap densities in perovskite thin films by employing electron-only or hole-only devices respectively[90,91]. SCLC requires the fabrication of multiple devices to characterize the density of electron traps or hole traps[88].

Furthermore, temperature-dependent SCLC measurements can be performed to determine the energetic level of the defects in the perovskite films. This technique usually probes the defect energy level close to both the conduction and valence bands by utilizing electron- and hole-only devices. The energy level EA of the defect can be measured using the expression:

$$E_A = \frac{d(\ln J)}{d(k_B T)^{-1}} \qquad (6)$$

Where T, J, and k_B are the absolute temperature, current density, and Boltzmann's constant, respectively. Adinolfi et al. conducted the temperature-dependent SCLC measurements to investigate the trap states close to conduction and valence bands in MAPbI$_3$ perovskite single crystal by employing electron-injecting and hole-injective devices, respectively, as shown in Fig. 17a-d. In the case of electron-injecting devices, titanium was

used on top of the perovskite layer to form an ohmic contact and favor electron injection. To determine the density of trap states as a function of energy, it is crucial to establish the relationship between voltage V and the energy levels of traps filled at the trap-filled limit voltage (V_{TFL}). This is accomplished by extracting the activation energy E_A from the temperature-dependent SCLC curves at various voltage points. The analysis revealed that the trap density exhibited energy localization, with a prominent peak observed at ~0.2 eV from the conduction band and another peak at around 0.1 eV from the valence band. These positions indicate the locations of the trap states, as shown in Fig. 17e[92].

Thermal admittance spectroscopy (TAS). TAS is employed to measure the distribution of defect density, including both shallow and deep-level defects, as a function of defect energy level within the bandgap of perovskite materials by tracing the junction capacitance. By varying the frequency of the applied AC voltage, the energy level of defects can be identified by monitoring the changes in capacitance. TAS measurements are conducted with the purpose of detecting the defect density and assessing the distribution of energy levels within the bandgap of semiconductors[14]. As shown in Fig. 18a, the electron trap states below the Fermi level are occupied by the photogenerated electrons. As the AC voltage frequency changes, charges stored within these traps are released within each cycle of the AC application, thereby contributing to the overall admittance. The probability of charge release is influenced by both the energy depth of the defect and the temperature, as thermal activation enables the charges to be released and further contributes to the admittance signal[93]. Consequently, traps with varying defect activation energies (E_A) at different temperatures and modulated AC frequencies are linked to the junction capacitance. Defective traps have the ability to capture or emit charges, thus influencing this capacitance. The defect density (N_T) can be determined from the capacitance that depends on the angular frequency according to the following relationship[34]:

$$N_T(E_\omega) = -\frac{V_{bi} \, dC \, \omega}{qW \, d\omega \, k_B T} \qquad (7)$$

Where C, ω, V_{bi}, W, k_B, and T are the capacitance, angular frequency, built-in potential, depletion region width, Boltzmann constant, and absolute temperature of the semiconductor, respectively. All these parameters are extracted using the capacitance-voltage (C-V), capacitance-frequency (C-f), and Mott-Schottky plots.
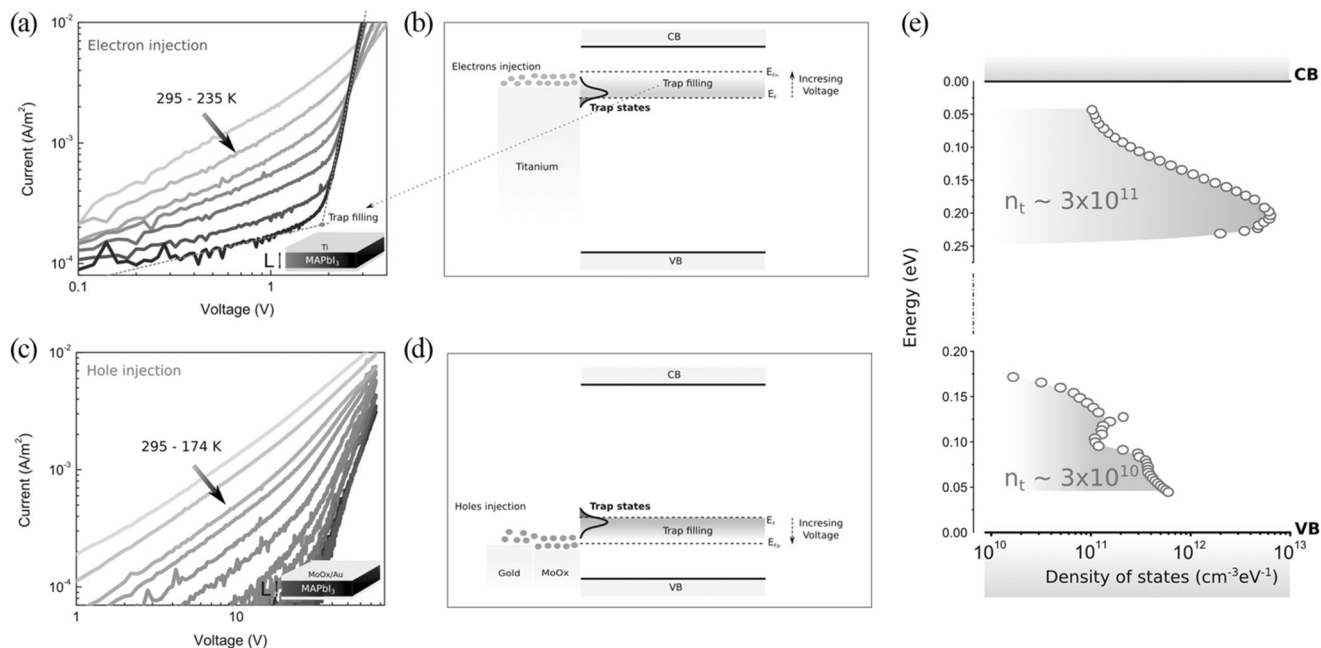
Fig. 17 Time-dependant SCLC measurement. a Temperature-dependent I-V curves for a MAPbI$_3$ single crystal. **b** Conceptual schematic of the SCLC method in the case of electron injection. **c** I-V curves vs temperature for a MAPbI$_3$ single crystal contacted using MoO$_3$/ Au/ Ag. **d** Conceptual schematic of the SCLC method in the case of hole injection. **e** The density of trap states within the bandgap was extracted from the temperature-dependent SCLC method. Reproduced with permission from ref. [92], copyright (Wiley-VCH Verlag GmbH and Co. KGaA, Weinheim, 2016).
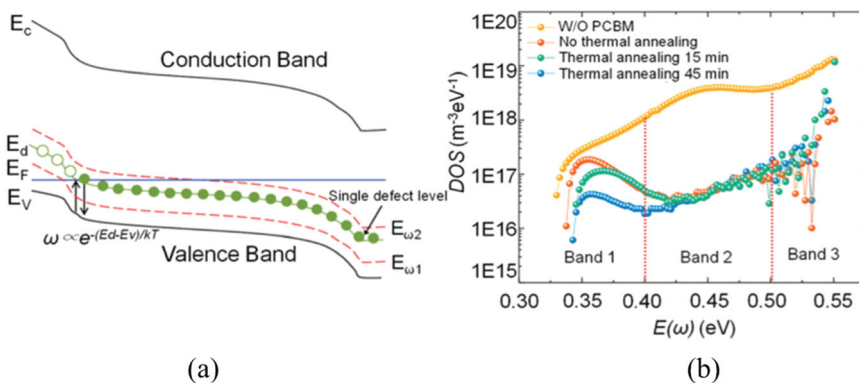

Fig. 18 Thermal admittance spectroscopy measurements for depicting the defect energetics. a p-Type semiconductor junction showing the filling of trap states below the Fermi level by photogenerated electrons[14]. Copyright 2015, Royal Society of Chemistry. **b** Typical trap density of states (*t-DOS*) plotted against defect energy level obtained by TAS measurements. Reproduced with permission from ref. [34], copyright (Springer Nature, 2014).

Shao et al. performed TAS measurements for the first time on MAPbI$_3$-based PSCs to investigate the underlying cause of hysteresis and its mitigation through fullerene passivation[34]. Fig. 18b depicts the density of states (t-DOS) plotted as a function of the defect energy level, E_o; three-band levels were obtained with a range of E_o values: band I (0.35–0.40 eV) and bands II and III (above 0.40 eV). Band I was indexed to a relatively shallow trap, while bands II and III were assigned to deeper-level defects. It was observed that all the[6,6]-phenyl-C$_{61}$-butyric acid methyl ester (PCBM)-modified devices exhibited significantly reduced deep traps when compared to devices without PCBM. Meanwhile, the annealed PCBM devices exhibited a further reduction in the shallow traps in comparison to unannealed PCBM devices. These findings suggest that deep traps predominantly exist at the surface of the perovskite film and can be effectively passivated by PCBM, even without the need for annealing. On the other hand, shallow traps are mainly concentrated at the grain boundaries and require annealing for the activation of PCBM-induced passivation at

these grain boundaries. Therefore, TAS is a qualitative method to compare the defect density in PSCs; however, it cannot distinguish between valence and conduction bands, which leads to an overestimation of defect density[94].

Deep-level transient spectroscopy (DLTS). DLTS allows for improved sensitivity, investigation of a wider range of defects at deeper energy levels within the bandgap, and ease of operation[95]. By capitalizing on the temperature-dependent fluctuations in defect emission rates, DLTS facilitates the determination of energy disparities between defect states and band edges. Additionally, DLTS enables the estimation of the cross-section of defects[96]. In DLTS measurement, variations in capacitance with temperature are measured to investigate the capacitance transients for temperatures ranging from liquid nitrogen temperature (between 63 and 77.2 K) to 300 K or above. When a bias pulse is applied at low temperatures, defects in the system become filled
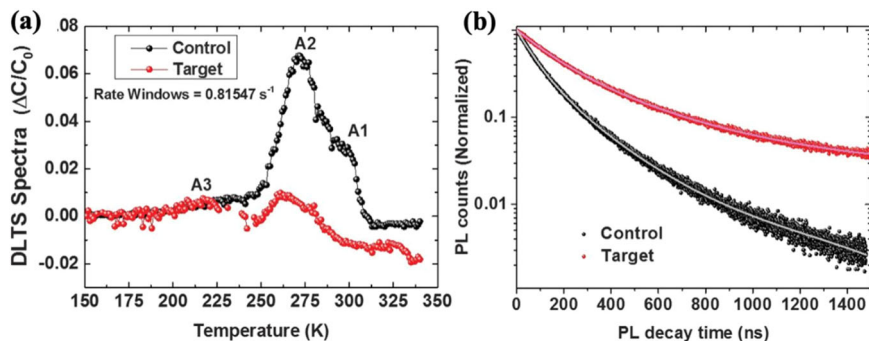
Fig. 19 Deep-level transient spectroscopy of FAPbI₃ perovskite devices. a DLTS spectra of triiodide ions treated FAPbI₃ films (target) (with the control) acquired in the temperature range of 150 to 330 K, **b** TRPL decay curves on the control and target perovskite films emitted at $\lambda = 825$ nm with the biexponential fitting. Reproduced with permission from ref. [97], copyright (American Association for the Advancement of Science, 2017).

by the charges generated by the applied bias. This occurs because the rate of capture for the defective traps is considerably higher than their emission rate at lower temperatures. With an increase in the temperature, DLTS peaks emerge when the emission rate of the trapped charges falls within the defined rate window. By completely filling the traps using a pulse of majority carriers or a saturating injection pulse, the capacitance undergoes a change, enabling the measurement of the defect density. At a particular temperature, trap density can be expressed as[95]

$$n_{trap} = 2(\triangle C/C)(N_A - N_D) \qquad (8)$$

Where $\triangle C$ is the change in capacitance from $t = 0$, and C is the capacitance of the diode under reverse-biased conditions. $(N_A - N_D)$ is the overall acceptor concentration on the p-side of the junction.

Yang et al. employed DLTS to quantify the density of deep-level defects within a FAPbI₃ perovskite film. The analysis revealed three DLTS peaks, each corresponding to specific defect energy levels. These peaks were observed at energy levels of 0.78 eV (A1), 0.82 eV (A2), and 0.46 eV (A3), as depicted in Fig. 19a[97]. In the FAPbI₃ film, all the identified energy levels were found to be positioned below the conduction band. These energy levels were associated with deep-level defects (A1 and A2) and semi-shallow defect (A3). The origin of these defects in the FAPbI3 film can be attributed to interstitial Pb (Pb$_i$) and antisite defects (MA$_I$, Pb$_I$, I$_{MA}$, and I$_{Pb}$). Interestingly, when the FAPbI₃ films were treated with triiodide ions, deep-level defects (A1 and A2) were no longer observed, resulting in a reduction in the overall concentration of defects. In addition, the triiodide-treated FAPbI₃ films displayed a longer carrier lifetime (1105 ns) in comparison to the control films (228 ns) (as shown in Fig. 19b, thus validating the decrease in the defect concentration. Furthermore, DLTS also provides information about the defect activation energy (E_A), concentration profile, and electron- and hole-capture cross-section of the different defects in halide perovskites. However, there are also some limitations associated with DLTS. In some cases, this technique may overlook minority charge traps that are unable to be filled under forward current conditions. Consequently, it only provides information about the energy level of defects and does not offer insights into the defect density[95].

Thermally stimulated current (TSC). In semiconductors, charges are trapped by defects that have a certain thermal activation energy; therefore, they can be released thermally. The features of the defects in the semiconductors can also be reflected by varying the current in the semiconductor. In principle, the thermally stimulated current (TSC) technique assumes partial filling of trap states by electrons that are optically excited at low temperatures. Subsequently, these electrons undergo thermal excitation in the

dark, transitioning into the conduction band minimum (CBM), which gives rise to the generation of a current signal, I_{TSC}. The activation energy (E_A) of the charge in the defect state is evaluated by the following equation:

$$I_{TSC} \propto \exp\left(-\frac{E_A}{k_B T}\right) \qquad (9)$$

Where I_{TSC} is the thermally simulated current, k_B is the Boltzmann constant, and T is the temperature.

The trap density (n_{trap}) can be calculated by integrating the TSC spectrum over a period of time using the following inequality:

$$S \int I_{TSC} dt \leq q n_{trap} V \qquad (10)$$

Where V refers to the volume of the sample.

For TSC measurements, the device is first cooled to an extremely low temperature, followed by the optical excitation of the charges[98]. Subsequently, the device is maintained at a constant low temperature to allow charges to undergo thermalization, relaxing into possible trap states within the density of states. By gradually increasing the temperature at a steady rate, charges are released from the defect traps, resulting in a current flow within the device, denoted as I_{TSC}. Baumann et al. utilized the TSC method to investigate defects in MAPbI₃ devices. In their study, two peaks (T₁ and T₂) were observed at very low temperatures, corresponding to shallow-level defect traps in the PCBM/C₆₀ electron transport layers. Additionally, a third peak (T3) was detected at a relatively higher temperature, which was ascribed to the phase transition of MAPbI₃ from orthorhombic to tetragonal phase, as shown in Fig. 20a. Notably, activation energies were found to be similar for all three device types, as presented in Fig. 20b: 488 meV without transport layers, 493 meV with the CuSCN HTL, and 528 meV with the PEDOT:PSS HTL. This analysis suggests the presence of relatively deep trap states at around 508 ± 20 meV in the MAPbI₃ film. Furthermore, a lower limit of 1×10^{21} cm^{-3} was calculated for the defect density using the time integral of TSC[99].

TSC has certain challenges associated with it that limit its applications. For instance, TSC measurements provide a lower limit estimation of the defect density. However, it is important to note that TSC may not detect certain defects due to factors such as partial detrapping of charges, incomplete trap filling, and recombination of the detrapped charges with carriers of the opposite charge.

Drive-level capacitance profiling (DLCP). The DLCP method was first employed in the study of amorphous silicon (Si), CuIn$_{1-x}$Ga$_x$Se₂, and Cu₂ZnSnSe₄ to examine the spatial
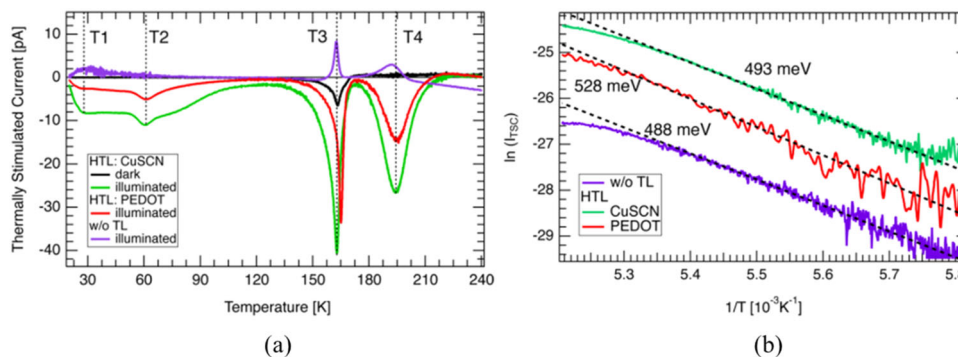
Fig. 20 Thermally stimulated current measurements of MAPbI3 perovskite devices. a TSC data of devices with and without hole transport layers in the dark and under illumination. **b** Arrhenius plots of the initial rise of the TSC peak T$_4$ for CuSCN and PEDOT:PSS HTL-based devices. Reproduced with permission from ref. [99], copyright (American Chemical Society, 2015).

distribution of trap states within these semiconductor materials[100–102]. From the junction capacitance measurements, DLCP enables the direct assessment of carrier density, including both the density of free carriers and the density of traps within the semiconductor's bandgap. Furthermore, DLCP provides information about the spatial and energetic distributions of these carriers and traps. DLCP provides higher resolution than any other technique because it provides flexibility to tune depletion region width by varying the applied voltage bias. However, non-flat depletion interfaces incurred either due to material heterogeneity or roughness impact the profiling.

Ni et al. applied the DLCP method to investigate the spatial and energetic distributions of trap states in single crystalline and polycrystalline metal halide PSCs[8]. Furthermore, each DLCP scan was completed within a few minutes, unlike DLTS measurements, where a long biasing time is required. When the DLCP measurement was performed on a single-crystal device based on MAPbI$_3$, it revealed that the density of traps near the interface region was approximately ten times higher compared to the trap density inside the MAPbI$_3$ single crystal. Therefore, it was concluded that the majority of traps are primarily situated on the crystal's surface, which could potentially be attributed to the existence of dangling bonds. Meanwhile, when DLCP measurements were conducted for MAPbI$_3$ thin single-crystal devices at different frequencies, it was observed that the junction capacitance increased as the AC frequency decreased. This observation indicates the existence of deep traps positioned on the surface of the thin MAPbI$_3$ single crystal. Trap density exhibited a declining trend as the profiling position was shifted from the interface to the bulk of the single crystal, indicating that the crystal's surface contained a majority of the trap states along with a higher concentration of carrier density. Figure 21a depicts a mapped image of the spatial and energetic distributions of the trap states in the MAPbI$_3$ thin single crystal as the profiling distance was scanned from the surface of the crystal towards the bulk.

Both DLCP and TAS techniques exhibited identical t-DOS spectra with characteristic trap bands located at E_ω values of 0.27 eV (band I), 0.35 eV (band II), and greater than 0.40 eV (band III). Therefore, it was concluded that deep traps were predominantly located at the surface of MAPbI$_3$ single crystals, while the bulk of single crystals contributed to shallower traps, as can be seen in Fig. 21a. Similarly, DLCP measurements performed on polycrystalline MAPbI$_3$-based PSCs also showed that deep trap states (trap band III) were mainly located close to the MAPbI$_3$/PTAA interface. Table 2 summarizes the minimum bulk trap density and interfacial trap density of the different perovskite films and single crystals measured using the DLCP method[8].

In a related investigation, Ni et al. combined the DLCP method with electrical poling to examine the charge states and resulting chemical properties of the mobile defects in the perovskite materials. Figure 21b shows the variations in the trap density of states of the MAPbI$_3$ thin single-crystal-based solar cell after applying a reverse bias of −1 V for different durations. It was observed that trap densities in both trap bands I and II progressively increased with longer biasing periods. The deep trap bands, band I (0.27 eV) and band II (0.36 eV), in MAPbI$_3$ were attributed to the presence of iodide interstitials (I_i^- and I_i^+), similar to FA$_x$Cs$_{1-x}$PbI$_3$ and FA$_x$MA$_{1-x}$PbI$_3$ perovskites. Figure 21c, d demonstrate the spatial distribution of trap densities for I_i^- and I_i^+ in FA$_{0.92}$Cs$_{0.08}$PbI$_3$ solar cells under both illumination and open-circuit conditions.

Ion migration and measurement methods

Since ion migration leads to hysteresis and degradation in device performance, it is important to understand and appropriately address ion migration[103]. The presence of mobile ionic vacancies screens the effective electric field inside the perovskite bulk layer. The lower electric field across the perovskite layer leads to inefficient extraction of photogenerated charge carriers[104]. Ion migration occurs due to the presence of ionic defects inside perovskite crystals. For MAPbI$_3$, among the three types of I^-, Pb^{2+}, and $CH_3NH_3^+$ vacancies, I^- vacancies have the highest concentration along with the lowest migration activation energy. Eames et al. calculated the activation energies for ionic migration in MAPbI$_3$ from first principles, compared these theoretical values with kinetic data extracted from the chronophotoamperometry measurements, and attributed the ion migration to originating primarily from iodide vacancies[104]. However, the exact mechanism of ion migration and its role in observed J–V hysteresis behavior are yet to be resolved completely. Some important characterization techniques to understand the spatial and temporal dynamics of ion migration during device operation have been discussed below.

Kelvin probe force microscopy (KPFM). KPFM can provide data about charge distribution and potential variation along the cross-section of PSCs. This data can be correlated with the position of different layers with up to 30 nm resolution. The KPFM probe tip first traces the surface topography using atomic force microscopy, and then the second pass follows the sample topography obtained from the first pass at a fixed height of tens of nanometers (lift mode)[105]. The distance between the sample and tip is kept such that electrostatic forces due to the contact potential difference (CPD) between the sample and tip become
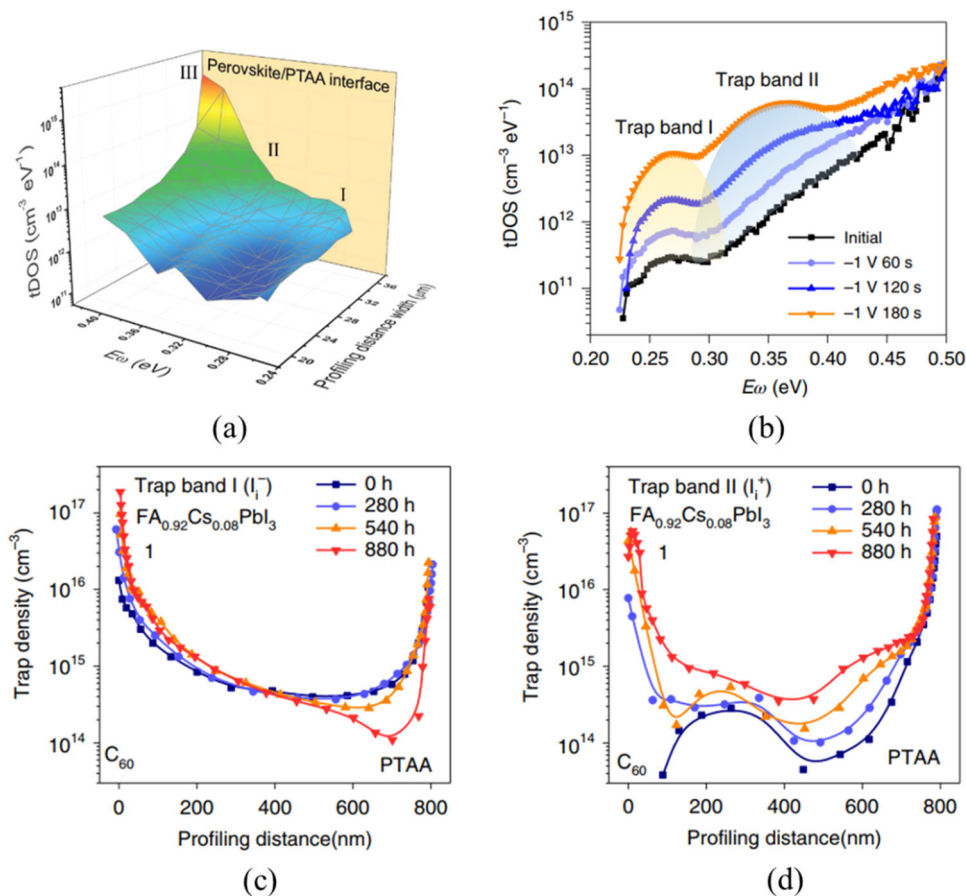
Fig. 21 Drive-level capacitance profiling measurements for spatial and energetic distribution of trap states in MAPbI₃ perovskites. a Mapped image of spatial and energetic distributions of densities of trap states in the MAPbI₃ single crystal, acquired using DLCP technique. Reproduced with permission from ref. [8], copyright (American Association for the Advancement of Science, 2020). **b** tDOS spectra of a MAPbI₃ thin single-crystal device before and after applying a reverse bias of −1 V for different time durations. Spatial duration of the trap densities of **c** trap band I and **d** trap band II in the FA$_{0.92}$Cs$_{0.08}$PbI$_3$ device after being illuminated at V$_{oc}$ condition for different duration of time. Reproduced with permission from ref. [131], copyright (American Association for the Advancement of Science, 2022).

Table 2 Comparison of the minimum bulk trap density and interfacial trap density between the different perovskite films and single crystals revealed using the DLCP technique.

Perovskite material	Minimal bulk trap density ($N_{T\ min}$) (cm^{-3})	Interface trap density (cm^{-3})	
MAPbBr₃ single crystal (bulk)	6.5×10^{10}	1.8×10^{12} (C$_{60}$)	1.8×10^{12} (Au)
MAPbI₃ single crystal (bulk)	1.8×10^{11}	1.2×10^{12} (C$_{60}$)	1.2×10^{12} (Au)
MAPbI₃ single crystal (thin)	1.9×10^{11} to 3.2×10^{12}	2.0×10^{13} to 1.1×10^{16} (C$_{60}$)	1.2×10^{12} to 1.0×10^{15} (PTAA)
Cs$_{0.05}$FA$_{0.70}$MA$_{0.25}$PbI$_3$ film	4.3×10^{14}	8.6×10^{15} (C$_{60}$)	1.2×10^{17} (PTAA)
Rb$_{0.05}$Cs$_{0.05}$FA$_{0.75}$MA$_{0.15}$Pb(I$_{0.95}$Br$_{0.05}$)$_3$ film	5.7×10^{14}	2.0×10^{16} (C$_{60}$)	1.1×10^{17} (PTAA)
FA$_{0.92}$MA$_{0.08}$PbI$_3$ film	7.9×10^{14}	1.9×10^{16} (C$_{60}$)	9.0×10^{16} (PTAA)
MAPbI₃ film	9.2×10^{14}	2.2×10^{16} (C$_{60}$)	1.2×10^{17} (PTAA)
Cs$_{0.05}$FA$_{0.8}$MA$_{0.15}$Pb$_{0.5}$Sn$_{0.5}$(I$_{0.85}$Br$_{0.15}$)$_3$ film	1.2×10^{15}	1.5×10^{16} (C$_{60}$)	1.1×10^{17} (PTAA)

Reproduced with permission from ref. [8], copyright (American Association for the Advancement of Science, 2020).

dominant over atomic forces. An AC drive voltage and variable DC bias are applied between the sample and tip during operation, and the CDP is obtained[106]. The frequency modulation mode of KPFM is preferred in most studies since it offers a higher spatial resolution.

Bergmann et al. conducted one of the first studies employing KPFM to understand space charge distribution inside PSCs[107]. By comparing the change in CPD before and after illumination, they were able to observe the accumulation of holes in front of the hole

transport layer. Such accumulation of holes within the cell could occur due to different charge carrier mobility in different materials or due to the difference in charge extraction efficiency between adjacent layers. To unravel the correlation between ion migration and interface effects, Weber et al. demonstrated a time-resolved KPFM (tr-KPFM) method to study the transient CPD in the PSCs (Fig. 22)[35]. The tr-KPFM method is based on decoupling the spatial mapping and recording the temporal evolution of the local CPD. The time resolution of sub-milliseconds was achieved using
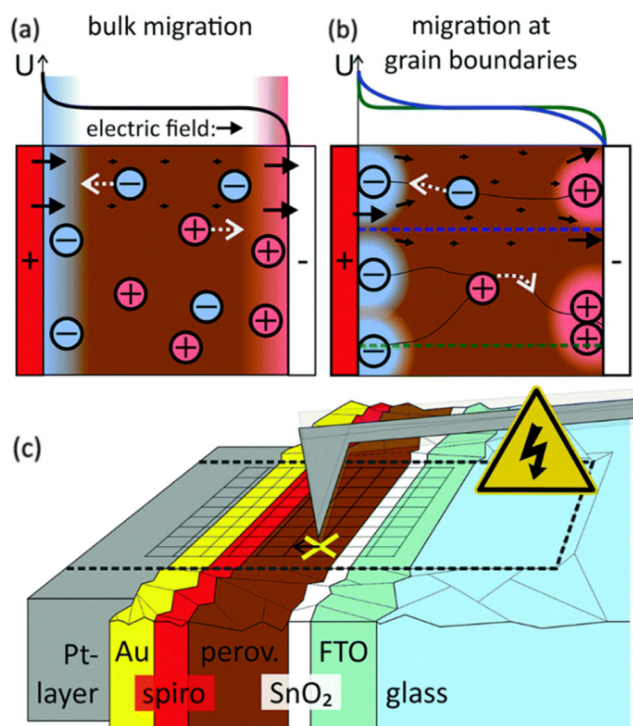
Fig. 22 Schematics of Kelvin probe force microscopy measurement. Illustration of potential (U), electric field (black arrows), and ion distribution: **a** Ion migration through the bulk of the perovskite layer forming uniform electrostatic double layers (EDLs) at both electrodes that screen the external device potential, **b** Ion migration preferentially at the grain boundaries form the non-uniform EDLs and heterogeneous electric field distribution, **c** In time-resolved KPFM, the CPD response to a voltage- or light-pulse is recorded at different positions on the sample. Reproduced with permission from ref. [35], copyright (Royal Society of Chemistry, 2018).

this method. Based on the observations, the authors concluded that as opposed to slow migration of mobile ions, interface formation and release of ionic charges are responsible for the observed hysteresis in PSCs. By employing enhanced sampling techniques and advanced KPFM methods, it is possible to extend the temporal resolution to the microsecond range.

To investigate the impact of grain boundaries (GBs) on ion migration, Shao et al. used a combination of electric poling, SEM-EDS, and conductive atomic force microscopy (c-AFM)[108]. Electric poling followed by SEM-EDS on GBs and bulk grains confirmed the formation of less perovskite at GBs. Thereafter c-AFM revealed a large current hysteresis at grain boundaries compared to grains, which indicates grain boundary dominant ion migration. Recently, Jakob et al. developed a method to improve the spatial resolution of KPFM down to 25 nm[105]. Instead of employing high-amplitude AC voltage, the researchers developed a technique that utilizes a field-effect transistor (FET) switch to toggle the electrical connection between the tip and sample on and off periodically. Additionally, they integrated this FET-switched KPFM with photoinduced force microscopy (PiFM) to simultaneously capture spatially resolved chemical information and surface potential mapping. This new technique can enable better visualization of the ion migration dynamics in PSCs and should be used more frequently.

Scanning electron microscopy- energy dispersive X-ray spectroscopy (SEM-EDS). SEM is used to obtain information about grain size distribution, surface morphology, and cross-section layer thickness of the perovskite layer in PSCs. EDS module of

SEM can be used to obtain the elemental distribution along the cross-section as well as information on ion migration and element diffusion between the adjacent layers.

To check the effect of polymer additives on the ion migration in MAPI PSCs, Li et al. used SEM-EDS to identify the spatial distribution of multiple ions in aged PSCs[109]. SEM-EDS spatial mapping of devices initially and after aging under illumination was compared to reveal the extensive spread of I^- and Pb^{2+} ions within the electron transport layer (ETL) and silver electrode. Furthermore, silver diffusion into the ETL was also observed, which highlighted the corrosive nature of ions originating from the perovskite layer. Similarly, to check the efficacy of their proposed ions-blocking layer (IBL), Li et al. utilized SEM-EDS on an inverted device structure (ITO/ P3CT-N / Perovskite/ IBL/ PCBM/ C_{60}/ TPBi/ Cu)[110]. In devices with severe ion migration, the I and Cu element distribution overlap could be observed from EDS. On the other hand, devices with suppressed ion migration possessed a clear boundary line between I and Cu signals.

Xing et al. developed a method based on SEM-EDS for direct measurement of halide ion migration activation energy[111]. To obtain the elemental contrast in EDS, a $PbBr_2$ particle of 2–5 μm size was placed on top of MAPI. EDS elemental mapping images of Br-element distribution, along with EDS line scans of Br-element under both dark and illumination conditions were compared. Direct visualization of increased Br^- diffusion after illumination was achieved since the $PbBr_2$ particle's boundary was blurred due to diffusion into the MAPI layer below. Figure 23 shows that ion migration was suppressed in the case of MAPI single crystals, whereas both heat and illumination led to increased Br^- migration into the underlying polycrystalline MAPI film. The line scan of the Br^- ion distribution was further analyzed to obtain the Br^- diffusivity and activation energy by following classical diffusion equations derived from Fick's laws.

Time-of-flight secondary ion mass spectrometry (ToF-SIMS). ToF-SIMS is a vacuum-based mass spectrometry technique used primarily to identify elemental, isotopic, and chemical components, by sputtering a confined and focused primary ion beam on the target. Surface atoms and molecular compounds from the target overcome the surface binding energy to form secondary ions (SIs). An electrostatic field accelerates the Sis, which are then transported to the detector over a drift path. These SIs are then detected by a time-of-flight (ToF) mass analyzer, as shown in Fig. 24a. ToF-SIMS can be used to study ion migration, interface composition, and degradation in PSCs. Dynamic SIMS can enable 3D analysis (both vertically and laterally) with high primary ion doses, rapid erosion rates, and a depth resolution of a few angstroms. Low ion dose in static SIMS can enable the measurement of elemental and molecular information while suppressing sample degradation with a spatial resolution of less than 50 nm over a surface[112]. DeQuilettes etal. used ToF-SIMS depth profiling to show that photo-irradiated films had low levels of iodide in the photo-irradiated area while adjacent areas had a higher level of iodide than the background concentration, suggesting a lateral migration of iodine away from the illuminated area[113].

Zhang et al. studied the ion migration effect by exposing PSCs to 5 h of continuous illumination followed by 2 weeks in the dark in a glovebox (0% R.H.). The device's performance was adversely affected not only by mobile iodide (I^-) ions from the perovskite layer diffusing out but also by Ag atoms/ions from the metal electrode diffusing into the perovskite layer, causing severe degradation in both $MAPbI_3$ and $FAPbI_3$ devices (Fig. 24b)[114]. Ion diffusion inside (outside) the HTL without an external electric field suggests that this process would be accelerated under an external electric field.
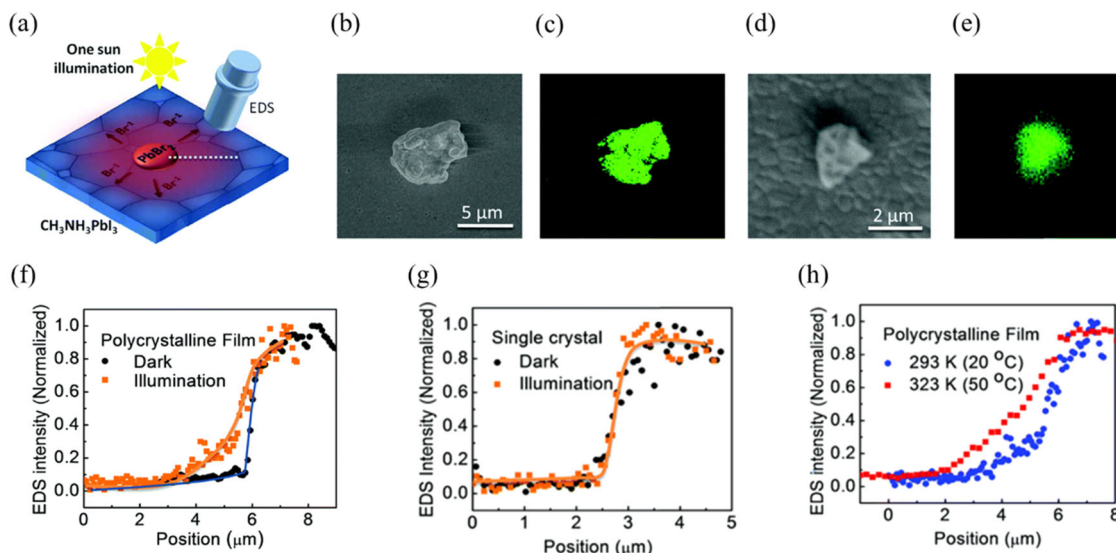
Fig. 23 Mapping ionic diffusion in MAPbI₃ perovskite films using Scanning electron microscopy and energy dispersive X-ray measurements. EDS study of Br diffusion in MAPI film, **a** Experimental setup for the ion diffusion study, **b**, **c** SEM and EDS Bromine-distribution images of a PbBr₂ particle without illumination, **d**, **e** SEM and EDS Bromine-distribution images of a PbBr₂ particle after illumination, The EDS line scans of the Br-element on the **f** MAPI polycrystalline film and **h** MAPI single crystal with and without illumination, **g** The EDS line scans of the Br element on the polycrystalline film under illumination at 293 and 323 K. Reproduced with permission from ref. [111], copyright (Royal Society of Chemistry, 2016).
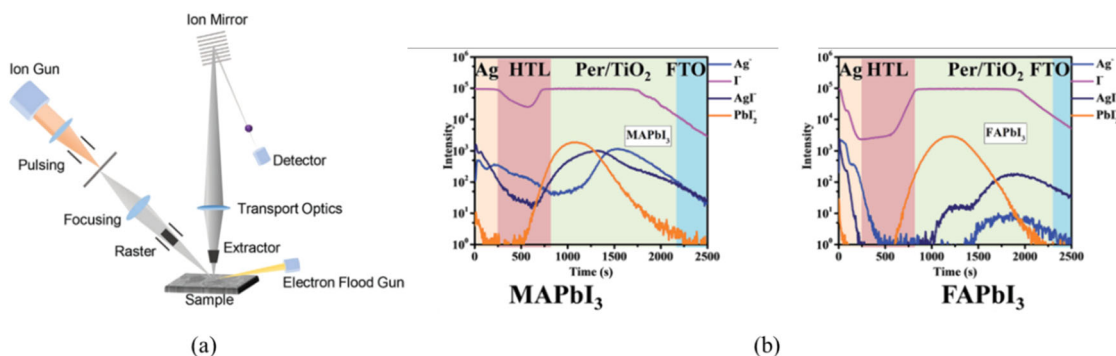

Fig. 24 Time-of-flight secondary ion mass measurements for ion migration study in perovskite films. a Principle of ToF-SIMS. Reproduced with permission[112]. Copyright 2020, Willey-VCH. **b** Evidence of ion migration in perovskite devices after degradation from continuous light illumination of AM 1.5G for 5 h: Elemental distribution across the devices from the cathode (Ag) to the anode (FTO), (i) MAPbI₃ device, (ii) FAPbI₃ device. Reproduced with permission from ref. [114], copyright (Royal Society of Chemistry, 2017).

Time-resolved time-of-flight secondary ion mass spectrometry (tr-ToF-SIMS) can be used to investigate the time evolution of ion distribution in perovskites under light illumination. Light-ON and OFF-field response was used with tr-ToF-SIMS to show that MA⁺ migration hysteresis is more illumination-dependent than I⁻ migration and allowed direct observation of the real-time dynamics of ions (such as MA⁺ and I⁻)[115].

Photothermal-induced resonance (PTIR). The static TOF-SIMS signal is strongly influenced by the chemical surroundings and is primarily sensitive to the top surface layer, typically a few nanometers in depth. In contrast, PTIR data can penetrate several hundred nanometers into the sample. The PTIR technique integrates the use of a pulsed infrared (IR) laser for excitation and an AFM operating in contact mode as a local detector. This allows for the measurement of the sample's expansion caused by light absorption. In PTIR measurements, a tunable laser beam is focused on a particular spot of the sample, which leads to thermal expansion, which is then measured as an oscillation of the AFM

cantilever. PTIR is particularly effective in measuring materials characterized by significant thermal expansion and low thermal conductivity[116]. PTIR can also measure the mechanical properties of the sample, like stiffness, elasticity, and damping, with nanometer-scale spatial resolution. The PTIR technique enables the mapping of chemical species distributions, such as MA⁺ in MAPbI₃, by leveraging IR spectroscopy to identify key moieties. Yuan et al. employed PTIR microscopy to map the spatial distribution of MA⁺ ions in MAPbI₃ perovskite. The authors confirmed that the migration of mobile ions induced doping in the perovskite film near the two electrodes. Figure 25a shows the representative PTIR spectra showcasing the IR absorption peaks corresponding to MA⁺ ions in the perovskite film. The AFM topography image and PTIR image of the CH₃ asymmetric deformation of the MA⁺ ion exhibit uniformity, as shown in Fig. 25b, c. Following electrical poling of the films with an electrical field of 1.6 V μm⁻¹ for 100 and 200 s, the topography images demonstrate no significant changes, as shown in Fig. 25d, f. However, the corresponding PTIR chemical maps in Fig. 25(e, g) reveal an increase in the MA⁺ absorption intensity in the vicinity
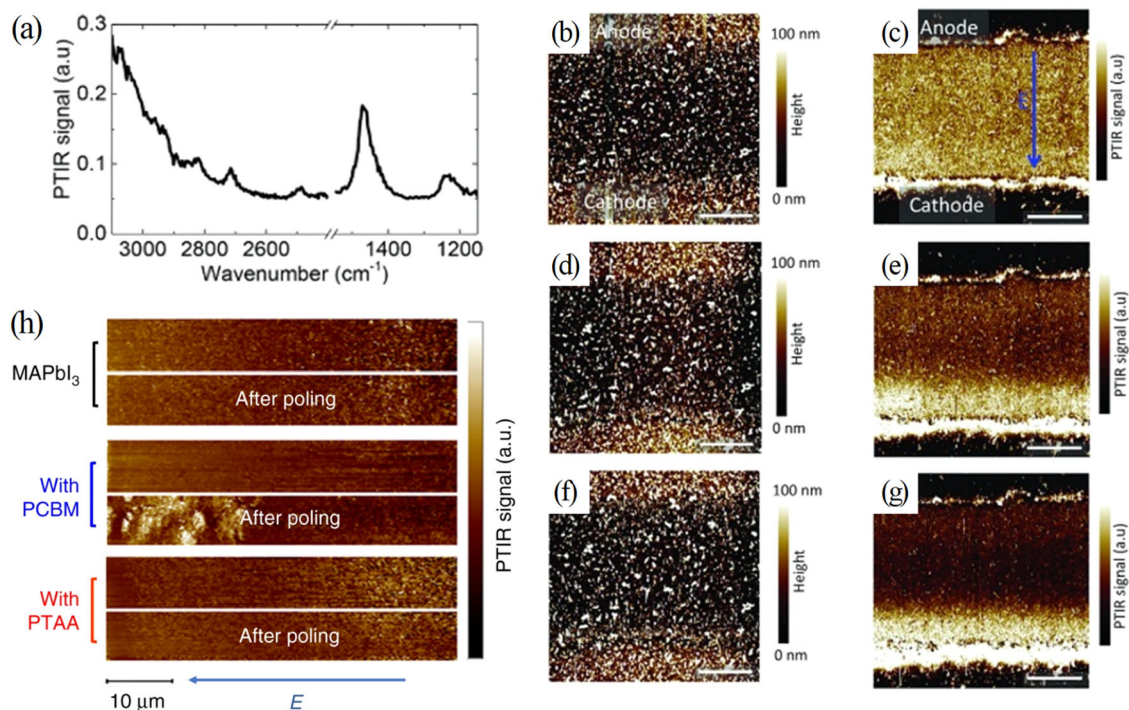
Fig. 25 Photothermal-induced resonance measurements for mapping elemental composition under illumination in MAPbI$_3$ perovskite films. a PTIR absorption spectrum recorded at the center of the MAPbI$_3$ device. Topography maps (80 μm × 80 μm) of the MAPbI$_3$ film of the same sample area before (**b**), after 100 s (**d**), and after 200 s (**f**) electrical poling, respectively. **c**, **e**, **g** Corresponding PTIR images for the CH$_3$ asymmetric deformation absorption of MA$^+$ ion obtained before (**c**), after 100 s (**e**), and after 200 s (**g**) electrical poling, respectively. All scale bars are 20 μm. Reproduced with permission from ref. [117], copyright (Wiley-VCH Verlag GmbH & Co. KGaA, Weinheim, 2015). **h** PTIR mapping of MAPbI$_3$ film as well as those covered by PCBM and PTAA, at the same location before and after poling under illumination. Reproduced with permission from ref. [132], copyright (Springer Nature, 2018).

of the cathode as a function of the poling time. These PTIR maps indicate redistribution of the MA$^+$ concentration due to electrical poling, providing direct evidence of MA$^+$ ion electromigration towards the negatively charged electrode.

Similarly, Lin et al. utilized PTIR microscopy to investigate the redistribution of organic cations during the poling process. In their study, PCBM-covered MAPbI$_3$ samples were subjected to poling under an electric field of 1 V μm^{-1} while being illuminated for 60 s (30 mW cm^{-2}, 532 nm). As a result, an observable increase in the content of MA$^+$ ions was identified at the cathode side, indicating the migration of MA$^+$ ions from the anode to the cathode, as shown in Fig. 25h. Yan et al. studied the ion migration effect on the lateral structure of perovskite using PTIR microscopy. It was observed that the MA$^+$ group displayed rapid rotational dynamics, characterized by a relaxation time of several picoseconds at room temperature. This observation suggested a weak interaction between MA$^+$ ions and the inorganic framework. Additionally, no redistribution of I$^-$ or Pb^{2+} ions was observed in the devices. However, in the presence of an electric field, a redistribution of MA$^+$ ions occurred. Due to increased strain caused by an applied field, the energy barrier for the ion migration (MA$^+$) was reduced, promoting device degradation[117,118].

Conclusions and outlook

Probing the bulk and surface defects in semiconductors using ultrafast spectroscopic characterization techniques has gained attention in recent times, leading to the development of several composite techniques. The investigation of crucial dynamic processes in semiconductors, including carrier recombination, trapping, and detrapping, involves the utilization of optical pump-probe techniques. These techniques employ a pulsed laser

and an optical delay to study these processes in detail. The probe radiation (THz wave) used in these techniques has low energy but possesses strong penetrating power. This characteristic enables the non-destructive detection of samples. While THz waves do not directly excite charges, they can induce oscillation or generate fundamental excitation in carriers. Furthermore, the sub-picosecond resolution enables detailed observation of the intricate interactions between defects and charge carriers in semiconductors. However, the data obtained from these ultrafast spectroscopic characterization techniques are highly sensitive to sample preparation and experimental setup; therefore, precautions should be taken during the handling of distinct perovskite samples. Pump-push-probe techniques offer several advantages, including the ability to manipulate the populations of excited state carriers and investigate the energetics and kinetics of electronic trap states in perovskite materials. However, the signal generated from the push-pulse can have interference from additional effects due to the distribution of hot carriers near the band edge, which must be subtracted to get the response from trapped carriers. While ultrafast techniques are well-suited for studying charge carrier dynamics in perovskite systems, their spatial resolution is limited to tens of microns due to the diffraction limit of the probe radiation, resulting in poor spatial resolution. Therefore, achieving spatial resolution better than 10 nm will further enhance the measurement accuracy of carrier dynamics on very short length and time scales. From the perspective of device characterization techniques, characterizing the charge-carrier dynamics of a functioning cell under specific voltage and illumination conditions still remains a challenge for the research community. Some of the electrical techniques, such as TAS and TSC, are unable to distinguish between conduction and valance band states, while others, such as SCLC and DLTS, have higher error margins, which could lead to inaccurate defect density

Table 3 Summary of different types of characterization techniques.

Technique name	Defect type	Fabrication stage	Features	Limitations	Ref.
Optical techniques					
Optical-pump terahertz-probe spectroscopy (OPTPS)	Overall defects	Substrate/ Perovskite	Accurate measurements of carrier density, mobility, and diffusion length Determination of recombination kinetics and rate constants	Insensitive to defect-related effects that impede the carrier motion over large distances	66–68,121
Pump-push-probe spectroscopy (PPPS)	Overall defects	Substrate/ Perovskite	Calculation of terahertz conductivity, charge carrier lifetime by varying push-pulse fluence	Temporal delay between the pump and push must be optimized to allow for pump-induced carriers to equilibrate to the band edge	72,122
Differential transient transmission spectroscopy (DTTS)	Interfacial defects	Glass/ HTL/ Perovskite	Investigation of the interfacial carrier dynamics to get hole and electron injection timelines from different charge transport materials	Optical absorption length of the excitation light should be shorter than the perovskite film thickness	71
Transient absorption (TA) spectroscopy	Bulk (deep) and surface (shallow) defects	Substrate/ Perovskite	Measurement of the total population of electrons and holes and their recombination behavior	Does not provide spatial distribution as it averages over a large region leading to incorrect interpretation of the spectrum	69
Transient photoluminescence (TRPL)	Bulk (deep) and surface (shallow) defects	Substrate/ Perovskite	Extraction of information about various competitive radiative and nonradiative recombination processes that occur in a system	Limited sensitivity based on film thickness. Requires complex measurements to accurately retrieve the parameter values	50
Transient absorption microscopy (TAM)	Spatial mapping of trap states	Substrate/ Perovskite	Contact-free and noninvasive method. Can quantify the spatial distribution of electronic excited states and traps. Can also map the emission propensity at the same spatial locations in the sample	Requires a spatially filtered pump and probe beam to remove unwanted high-order spatial modes. Spatial filtering is critical for achieving diffraction-limited beam sizes	44
Ultrafast photocurrent spectroscopy (UPS)	Ultra-shallow to shallow defects	Substrate/ Perovskite/ Au	Eliminates scattering and reflection artefacts giving it an outstanding dynamic range, sufficient for the identification of very low concentrations of defect states and intermolecular interactions	Steady-state technique incapable of addressing and resolving in time, the dynamics of the excited states	69
Transient photoluminescence microscopy (TRPLM)	Bulk (deep) and surface (shallow) defects	Substrate/ Perovskite	Background-free imaging method and is more sensitive than transient absorption. Has the advantage over TAM for imaging carrier diffusion over nanosecond or longer time scales when the TA signal is low and more susceptible to noise	Low temporal resolution (sub-nanosecond) compared to TAM is limited by the response time of the detectors	71
					75

Table 3 (continued)

Technique name	Defect type	Fabrication stage	Features	Limitations	Ref.
Time-resolved microwave conductivity (TRMC)	Bulk (deep) and surface (shallow) defects	Substrate/ Perovskite	Evaluation of charge carrier transport properties Direct evidence of trap-mediated decay in photoconductivity	Low time resolution in the photoconductivity measurements	
Photoinduced charge extraction by linearly increasing the voltage (Photo-CELIV)	Overall defects	Substrate/ Perovskite/ Au (or Ag)	Accurate measurement of charge carrier mobility Investigation of bulk charge transport in perovskite films	Only qualitative analysis of trap states	123
Time-resolved Kerr Rotation (TRKR)	Overall defects	Substrate/ Perovskite	Study of coherent spin dynamics in perovskite materials; calculation of Landè factor (g) of charge carriers Measurement of anisotropic thermal conductivity in thin films	Difficult to resolve the different KR signals originating from weakly localized charge carriers	81
Absolute photoluminescence quantum yield (APQY)	Bulk and interfacial defects	Substrate/ Perovskite	Investigation of recombination regimes in the perovskite films as a function of optically injected carrier concentration Evaluation of optoelectronic quality of perovskite films	Poor signal-to-noise ratios have a significant effect on the recorder APLQY values	84
Sub-bandgap external quantum efficiency (s-EQE)	Shallow and deep defects	Complete device	Information about the sub-band states such as traps and energetic disorder in perovskite materials Versatile technique used to study solar cells under electrical and light bias	Need to reduce the electrical and optical noise in the response data	85
Electrical techniques					
Deep-level capacitance profiling (DLCP)	Shallow and deep defects	Complete device	Measures spatial and energetic distribution of trap throughout the perovskite layer Measures both the shallow and deep defects at the same time, gives activation energy, and provides higher resolution to defect evaluation than any other technique	Complicated setup, difficult to extract data	8
Deep-level transient spectroscopy (DLTS)	Shallow and deep defects	Complete device	Extremely sensitive, a wide range of defects depths can be probed. Information about electron and hole-capture coefficients can be obtained	Sometimes misses minority carrier traps which cannot be saturated at practical levels of forward current Unable to trace shallow-level defects which have higher thermal emission rate	124

Table 3 (continued)

Technique name	Defect type	Fabrication stage	Features	Limitations	Ref.
Thermally stimulated current (TSC)	Shallow and deep defects	Complete device	A wide range of defect levels can be probed by tracing thermally activated current, information about the activation energy of defects Can be performed under illumination on regular working solar cells	Unable to distinguish between the valence band and conduction band states, only the lower limit of defect density can be evaluated, trapped charges having long thermal emission time do not contribute to a thermally activated current signal	99,125
Space-charge limited current (SCLC)	Overall defects	Electron- or hole-only device	Information about two types of defect density, i.e., electron and hole density, temperature-dependent SCLC gives activation energy of defects	Only one type of defect density at one time can be measured, deviation in estimated defect density due to difficulty in accurate determination of kink point of VTFL, need fabrication of two types of an electron as well as hole-only devices	38,89,91,126
Thermal admittance spectroscopy (TAS)	Shallow and deep defects	Complete device	Shallow and deep traps can be obtained by tracing the junction capacitance, and the activation energy of the defects can be calculated and can be performed on the complete device under dark and illumination	Unable to distinguish between the valence band and conduction band states, only defects with the energy below the energy demarcation can contribute to the capacitance signal, trapped charges with long thermal emission time cannot contribute to the capacitance signal	127–129
Ion migration techniques					
Kelvin probe force microscopy (KPFM)	Ionic vacancies	Complete device, cross-section profile, Au/ Perovskite/ Au also used sometimes	Information about the direction and extent of ion migration. Usually, electric poling is done in a particular direction to segregate ions, thereafter the changes in the work function of ETL/perovskite or perovskite/ HTL interface are analysed. Enables mapping of the spatial and temporal evolution of the electric field in the device. It could be used to study the time dependence of ion migration with sub-millisecond resolution. High spatial resolution up to 30 nm is achievable.	Sample preparation can be challenging, high voltage needs to be applied between the probe tip and sample surface for better resolution, which can lead to artefacts or damage to the sample surface	35,106–108

Table 3 (continued)

Technique name	Defect type	Fabrication stage	Features	Limitations	Ref.
Scanning electron microscope- energy dispersive X-ray spectroscopy	Ionic vacancies	Complete device, substrate/ perovskite	Can identify the type of ion present at a particular location within the perovskite layer (e.g., ionic vacancies at grain boundaries). Information on the ion concentration gradient, ion accumulation, and stray ion migration from HTL into perovskite. Performed along with electric poling sometimes to check the effect of external electric field on ion migration	Sample preparation can be challenging and destructive Does not give an idea of ion migration dynamics	109-111
Photothermal-induced resonance (PTIR)	Ionic vacancies	Complete device	Information on the ion concentration gradient	High thermal expansion and low thermal conductivity materials are generally easy to measure with PTIR	116
Time-of-flight secondary ion mass spectrometry (ToF-SIMS)	Ionic vacancies	Complete device	Information on the ion concentration gradient	Only sensitive to the top surface layer.	130

measurements. Moreover, techniques such as DLCP have not been explored enough because the data extraction and analysis are rigorous and complicated. Therefore, efforts should be focused on developing a framework to improve the data extraction capability, which would help in the widespread adoption of DLCP. In tr-KPFM, by employing a faster sampling rate of AFM, temporal resolution in the microsecond range could be obtained, which would allow for a better mechanistic understanding of ion migration in PSCs. Since ion migration is one of the key reasons for the intrinsic instability of perovskites, a deeper understanding of the underlying mechanism can help mitigate ion migration and therefore bolster the ambient stability of PSCs. Additionally, in-situ methods that can monitor ion migration in real time are also scarce. Some of the ion migration techniques, such as c-AFM and SEM-EDS, involve intensive sample preparation techniques and are destructive in nature, which limits their application. Therefore, user-friendly techniques involving easier sample preparation or that are non-destructive would enable wider adoption and more data to be generated. One of the ways to estimate measurement errors, especially in electrical methods, is by calculating parameters such as defect density using ultrafast optical techniques, which would help understand the shortcomings of the other measurement techniques. This would facilitate the generation of reliable data and contribute to a deeper understanding of the underlying physics, robust model generation, and accurate directions for the improvement of device performance and stability.

Future advancements in perovskite device performance heavily rely on endeavors to comprehensively understand, identify, and regulate the bulk and interfacial defects within the perovskite materials. These defects play a crucial role in nonradiative recombination processes and have a significant impact on band alignment. In addition, the instability of perovskite materials under ambient conditions is a major hindrance in the long-term application and commercialization of perovskite devices. A better understanding of charge carrier dynamics, as well as fabrication procedures to fabricate defect-free structures, need to be developed to further improve the power conversion efficiency. The device performance can be adversely affected by interfaces, grain boundaries, and ion migration, which highlights the need for meticulous engineering of these defect structures to overcome their detrimental effects. Furthermore, defect passivation techniques such as additive engineering, compositional optimization, and interfacial modification must be developed to suppress the defect concentration and improve the device's performance. To establish the efficacy of these defect passivation techniques, it is imperative to measure the defect density accurately before and after treatment. Moreover, time- and spatially resolved measurements of defect density are also needed in solar cells to investigate the degradation mechanisms and mitigate the degradation pathways. In this regard, this review will play a significant role in informing the research community about the suitability of different characterization methods for the measurement of defect states directly and/or studying the charge carrier dynamics in perovskite materials. Table 3 summarizes different characterization techniques along with their features and limitations. It highlights which techniques reveal the time-resolved concentration of carriers (indicating the rate of recombination) while also indicating the techniques that provide the spatial distribution of defects. The table also identifies the techniques that have sensitivity for very low defect concentrations, while pointing out the ones that are only useful when the defect concentrations are reasonably high. Therefore, this table provides a comprehensive overview of the advantages, disadvantages, and appropriate use case scenarios for each of these techniques. We anticipate that this review will be instrumental for the researchers in this field,

serving as an initial guide to help answer the question, i.e., Which defect characterization technique is most suitable for my research?

References

1. Tailor, N. K. et al. The effect of dimensionality on the charge carrier mobility of halide perovskites. *J. Mater. Chem. A* **9**, 21551–21575 (2021).
2. Sahare, S. et al. Emerging perovskite solar cell technology: remedial actions for the foremost challenges. *Adv. Energy Mater.* **11**, 2101085 (2021).
3. Pham, H. D. et al. Organic interfacial materials for perovskite-based optoelectronic devices. *Energy Environ. Sci.* **12**, 1177–1209 (2019).
4. Kim, M. et al. Conformal quantum dot–SnO2 layers as electron transporters for efficient perovskite solar cells. *Science* **375**, 302–306 (2022).
5. Ranjan, R. et al. Enhanced thermal and moisture stability via dual additives approach in methylammonium lead iodide based planar perovskite solar cells. *Solar Energy* **225**, 200–210 (2021).
6. Zhang, H. et al. A universal co-solvent dilution strategy enables facile and cost-effective fabrication of perovskite photovoltaics. *Nat. Commun.* **13**, 89 (2022).
7. Saidaminov, M. I. et al. Planar-integrated single-crystalline perovskite photodetectors. *Nat. Commun.* **6**, 8724 (2015).
8. Ni, Z. et al. Resolving spatial and energetic distributions of trap states in metal halide perovskite solar cells. *Science* **367**, 1352–1358 (2020). **Spatial and energetic distributions of trap states in metal halide perovskite using drive-level capacitance profiling**.
9. Yuan, Y. & Huang, J. Ion migration in organometal trihalide perovskite and its impact on photovoltaic efficiency and stability. *Acc. Chem. Res.* **49**, 286–293 (2016).
10. Leijtens, T. et al. Carrier trapping and recombination: the role of defect physics in enhancing the open circuit voltage of metal halide perovskite solar cells. *Energy Environ. Sci.* **9**, 3472–3481 (2016).
11. Wetzelaer, G.-J. A. H. et al. Trap-assisted non-radiative recombination in organic–inorganic perovskite solar cells. *Adv. Mater.* **27**, 1837–1841 (2015).
12. Xiao, Z. et al. Giant switchable photovoltaic effect in organometal trihalide perovskite devices. *Nat. Mater.* **14**, 193–198 (2015).
13. Ranjan, R. et al. Role of PC60BM in defect passivation and improving degradation behaviour in planar perovskite solar cells. *Solar Energy Mater. Solar Cells* **207**, 110335 (2020).
14. Duan, H.-S. et al. The identification and characterization of defect states in hybrid organic–inorganic perovskite photovoltaics. *Phys. Chem. Chem. Phys.* **17**, 112–116 (2015).
15. Correa-Baena, J.-P. et al. Promises and challenges of perovskite solar cells. *Science* **358**, 739–744 (2017).
16. Leijtens, T. et al. Towards enabling stable lead halide perovskite solar cells; interplay between structural, environmental, and thermal stability. *J. Mater. Chem. A* **5**, 11483–11500 (2017).
17. Jena, A. K., Kulkarni, A. & Miyasaka, T. Halide perovskite photovoltaics: background, status, and future prospects. *Chem. Rev.* **119**, 3036–3103 (2019).
18. Bryant, D. et al. Light and oxygen induced degradation limits the operational stability of methylammonium lead triiodide perovskite solar cells. *Energy Environ. Sci.* **9**, 1655–1660 (2016).
19. Yang, J. et al. Comprehensive understanding of heat-induced degradation of triple-cation mixed halide perovskite for a robust solar cell. *Nano Energy* **54**, 218–226 (2018).
20. Yun, J. S. et al. Humidity-induced degradation via grain boundaries of HC(NH2)2PbI3 planar perovskite solar cells. *Adv. Funct. Mater.* **28**, 1705363 (2018).
21. Christians et al. Transformation of the excited state and photovoltaic efficiency of CH3NH3PbI3 perovskite upon controlled exposure to humidified air. *J. Am. Chem. Soc.* **137**, 1530–1538 (2015).
22. Aristidou, N. et al. Fast oxygen diffusion and iodide defects mediate oxygen-induced degradation of perovskite solar cells. *Nat. Commun.* **8**, 15218 (2017).
23. Domanski, K. et al. Migration of cations induces reversible performance losses over day/night cycling in perovskite solar cells. *Energy Environ. Sci.* **10**, 604–613 (2017).
24. Conings, B. et al. Intrinsic thermal instability of methylammonium lead trihalide perovskite. *Adv. Energy Mater.* **5**, 1500477 (2015).
25. Ranjan, R. et al. Enhanced efficiency and thermal stability of mesoscopic perovskite solar cells by adding PC70BM acceptor. *Solar Energy Mater. Solar Cells* **202**, 110130 (2019).
26. Buin, A. et al. Materials processing routes to trap-free halide perovskites. *Nano Lett.* **14**, 6281–6286 (2014).
27. Yin, W.-J., Shi, T. & Yan, Y. Unusual defect physics in CH3NH3PbI3 perovskite solar cell absorber. *Appl. Phys. Lett.* **104**, 063903 (2014).
28. Kim, N.-K. et al. Investigation of thermally induced degradation in CH3NH3PbI3 perovskite solar cells using in-situ synchrotron radiation analysis. *Sci. Rep.* **7**, 1–9 (2017).
29. Queisser, H. J. & Haller, E. E. Defects in semiconductors: some fatal, some vital. *Science* **281**, 945–950 (1998).
30. Kim, J. et al. The role of intrinsic defects in methylammonium lead iodide perovskite. *J. Phys. Chem. Lett.* **5**, 1312–1317 (2014).
31. Agiorgousis, M. L. et al. Strong covalency-induced recombination centers in perovskite solar cell material CH3NH3PbI3. *J. Am. Chem. Soc.* **136**, 14570–14575 (2014).
32. Buin, A. et al. Halide-dependent electronic structure of organolead perovskite materials. *Chem. Mater.* **27**, 4405–4412 (2015).
33. Walsh, A. et al. Self-regulation mechanism for charged point defects in hybrid halide perovskites. *Angew. Chem. Int. Ed.* **127**, 1811–1814 (2015).
34. Shao, Y. et al. Origin and elimination of photocurrent hysteresis by fullerene passivation in CH3NH3PbI3 planar heterojunction solar cells. *Nat. Commun.* **5**, 1–7 (2014).
35. Weber, S. A. et al. How the formation of interfacial charge causes hysteresis in perovskite solar cells. *Energy Environ. Sci.* **11**, 2404–2413 (2018). **Time-resolved KPFM method to map and track the potential distribution in perovskite solar cells with sub-ms resolution**.
36. Saidaminov, M. I. et al. Suppression of atomic vacancies via incorporation of isovalent small ions to increase the stability of halide perovskite solar cells in ambient air. *Nat. Energy* **3**, 648–654 (2018).
37. Kim, M. et al. Methylammonium chloride induces intermediate phase stabilization for efficient perovskite solar cells. *Joule* **3**, 2179–2192 (2019).
38. Ranjan, S. et al. Low-temperature microwave processed TiO2 as an electron transport layer for enhanced performance and atmospheric stability in planar perovskite solar cells. *ACS Appl. Energy Mater.* **5**, 2679–2696 (2022).
39. Ball, J. M. & Petrozza, A. Defects in perovskite-halides and their effects in solar cells. *Nat. Energy* **1**, 1–13 (2016).
40. Patrizi, B. et al. Synergistic approach of ultrafast spectroscopy and molecular simulations in the characterization of intramolecular charge transfer in push-pull molecules. *Molecules* **25**, 430 (2020).
41. Jiang, X. et al. Transient sub-band-gap states at grain boundaries of CH3NH3PbI3 perovskite act as fast temperature relaxation centers. *ACS Energy Lett.* **4**, 1741–1747 (2019).
42. Meggiolaro, D. et al. Iodine chemistry determines the defect tolerance of lead-halide perovskites. *Energy Environ. Sci.* **11**, 702–713 (2018).
43. Gao, C.-H. et al. TiI4-doping induced bulk defects passivation in halide perovskites for high efficient photovoltaic devices. *Org. Electron.* **88**, 105973 (2021).
44. Narra, S. et al. Femtosecond transient absorption spectra and dynamics of carrier relaxation of tin perovskites in the absence and presence of additives. *J. Phys. Chem. Lett.* **11**, 5699–5704 (2020).
45. Motti, S. G. et al. Defect activity in lead halide perovskites. *Adv. Mater.* **31**, 1901183 (2019).
46. Xin, C. et al. Defects healing in two-step deposited perovskite solar cells via formamidinium iodide compensation. *ACS Appl. Energy Mater.* **3**, 3318–3327 (2020). **Passivation of defects along the grain boundaries in perovskite solar cells by post-treatment of FAI solution in IPA as revealed via TAS and TRPL measurements**.
47. Snaider, J. M. et al. Ultrafast imaging of carrier transport across grain boundaries in hybrid perovskite thin films. *ACS Energy Lett.* **3**, 1402–1408 (2018). **Spatial and temporal imaging of sub-bandgap states within and across the grain boundaries in hybrid perovskite thin films**.
48. Simpson, M. J. et al. Imaging electronic trap states in perovskite thin films with combined fluorescence and femtosecond transient absorption microscopy. *J. Phys. Chem. Lett.* **7**, 1725–1731 (2016).
49. Chen, X. et al. Identifying, understanding and controlling defects and traps in halide perovskites for optoelectronic devices: a review. *J. Phys. D Appl. Phys.* **53**, 373001 (2020).
50. Pean, E. V. et al. Interpreting time-resolved photoluminescence of perovskite materials. *Phys. Chem. Chem. Phys.* **22**, 28345–28358 (2020).
51. Jones, T. W. et al. Lattice strain causes non-radiative losses in halide perovskites. *Energy Environ. Sci.* **12**, 596–606 (2019).
52. Alarousu, E. et al. Ultralong radiative states in hybrid perovskite crystals: compositions for submillimeter diffusion lengths. *J. Phys. Chem. Lett.* **8**, 4386–4390 (2017).
53. Peters, J. A. et al. Carrier recombination mechanism in CsPbBr3 revealed by time-resolved photoluminescence spectroscopy. *Phys. Rev. B* **100**, 235305 (2019).

54. Ghosh, S. et al. Light-induced defect healing and strong many-body interactions in formamidinium lead bromide perovskite nanocrystals. *J. Phys. Chem. Lett.* **11**, 1239–1246 (2020).

55. Kirchartz, T. et al. Photoluminescence-based characterization of halide perovskites for photovoltaics. *Adv. Energy Mater.* **10**, 1904134 (2020).

56. Scheblykin, I. G. Small number of defects per nanostructure leads to "digital" quenching of photoluminescence: the case of metal halide perovskites. *Adv. Energy Mater.* **10**, 2001724 (2020).

57. Baloch, A. A. B. et al. Analysis of photocarrier dynamics at interfaces in perovskite solar cells by time-resolved photoluminescence. *J. Phys. Chem. C* **122**, 26805–26815 (2018).

58. Yamada, Y. et al. Spontaneous defect annihilation in CH3NH3PbI3 thin films at room temperature revealed by time-resolved photoluminescence spectroscopy. *J. Phys. Chem. Lett.* **6**, 482–486 (2015).

59. Wen, X. et al. Defect trapping states and charge carrier recombination in organic–inorganic halide perovskites. *J. Mater. Chem. C* **4**, 793–800 (2016).

60. Dobrovolsky, A. et al. Relating defect luminescence and nonradiative charge recombination in MAPbI3 perovskite films. *J. Phys. Chem. Lett.* **11**, 1714–1720 (2020).

61. Jiang, Y. et al. Time-resolved fluorescence anisotropy study of organic lead halide perovskite. *Solar Energy Mater. Solar Cells.* **151**, 102–112 (2016).

62. Tian, Y. et al. Enhanced organo-metal halide perovskite photoluminescence from nanosized defect-free crystallites and emitting sites. *J. Phys. Chem. Lett.* **6**, 4171–4177 (2015).

63. Shi, J. et al. From ultrafast to ultraslow: charge-carrier dynamics of perovskite solar cells. *Joule* **2**, 879–901 (2018).

64. Zhao, D. & Chia, E. E. Free carrier, exciton, and phonon dynamics in lead-halide perovskites studied with ultrafast terahertz spectroscopy. *Adv. Opt. Mater.* **8**, 1900783 (2020).

65. Johnston, M. B. & Herz, L. M. Hybrid perovskites for photovoltaics: charge-carrier recombination, diffusion, and radiative efficiencies. *Acc. Chem. Res.* **49**, 146–154 (2016).

66. Wehrenfennig, C. et al. Charge-carrier dynamics in vapour-deposited films of the organolead halide perovskite CH 3 NH 3 PbI 3− x Cl x. *Energy Environ. Sci.* **7**, 2269–2275 (2014).

67. Rehman, W. et al. Charge-carrier dynamics and mobilities in formamidinium lead mixed-halide perovskites. *Adv. Mater.* **27**, 7938–7944 (2015). **Study of charge carrier dynamics in FAPb(Br$_y$I$_{1-y}$)$_3$ perovskite films using optical pump-probe spectroscopy**.

68. Yoo, J. J. et al. Efficient perovskite solar cells via improved carrier management. *Nature* **590**, 587–593 (2021). **Enhancement in the charge carrier mobility (~ 11 × 10^{-4} cm^{2}V^{-1}s) in MAPbI$_3$ perovskite using iodide additive as revealed from the photo-CELIV measurements**.

69. Kobbekaduwa, K. et al. In-situ observation of trapped carriers in organic metal halide perovskite films with ultra-fast temporal and ultra-high energetic resolutions. *Nat. Commun.* **12**, 1–7 (2021).

70. Tahara, H. et al. Experimental evidence of localized shallow states in orthorhombic phase of CH3NH3PbI3 perovskite thin films revealed by photocurrent beat spectroscopy. *J. Phys. Chem. C* **120**, 5347–5352 (2016).

71. Ishioka, K. et al. Direct observation of ultrafast hole injection from lead halide perovskite by differential transient transmission spectroscopy. *J. Phys. Chem. Lett.* **8**, 3902–3907 (2017).

72. Pollock, T. P. & Schlenker, C. W. Charge trapping dynamics revealed in CH3NH3PbI3 by ultrafast multipulse spectroscopy. *J. Phys. Chem. C* **125**, 18834–18840 (2021).

73. Venkatesan, N. R., Labram, J. G. & Chabinyc, M. L. Charge-carrier dynamics and crystalline texture of layered Ruddlesden–Popper hybrid lead iodide perovskite thin films. *ACS Energy Lett.* **3**, 380–386 (2018).

74. Yao, F. & Lin, Q. Charge carrier dynamics of organic cation-treated perovskites probed with time-resolved microwave conductivity. *ACS Photon.* **9**, 3165–3171 (2022).

75. Savenije, T. J. et al. Quantifying charge-carrier mobilities and recombination rates in metal halide perovskites from time-resolved microwave photoconductivity measurements. *Adv. Energy Mater.* **10**, 1903788 (2020). **Evidence of deep trap states (~ 500meV) present in the MAPbI$_3$ perovskite films calculated via thermally stimulated current measurements**.

76. Stephen, M. et al. Charge transport and its characterization using photo-CELIV in bulk heterojunction solar cells. *Polym. Int.* **66**, 13–25 (2017).

77. Laskar, M. A. R. et al. Phenylhydrazinium iodide for surface passivation and defects suppression in perovskite solar cells. *Adv. Funct. Mater.* **30**, 2000778 (2020).

78. Fukuoka, D. et al. Spin dynamics of two-dimensional electrons in a quantum Hall system probed by time-resolved Kerr rotation spectroscopy. *Phys. Rev. B* **78**, 041304 (2008).

79. Syperek, M. et al. Spin coherence of holes in GaAs/(Al, Ga) As quantum wells. *Phys. Rev. Lett.* **99**, 187401 (2007).

80. Kirstein, E. et al. Spin dynamics of electrons and holes interacting with nuclei in MAPbI3 perovskite single crystals. *ACS Photon.* **9**, 1375–1384 (2022).

81. Kirstein, E. et al. Lead-dominated hyperfine interaction impacting the carrier spin dynamics in halide perovskites. *Adv. Mater.* **34**, 2105263 (2022).

82. Faulkner, D. O. et al. Measurement of absolute photoluminescence quantum yields using integrating spheres–Which way to go? *Laser Photon. Rev.* **6**, 802–806 (2012).

83. Porres, L. et al. Absolute measurements of photoluminescence quantum yields of solutions using an integrating sphere. *J. Fluoresc.* **16**, 267–273 (2006).

84. Sutter-Fella, C. M. et al. High photoluminescence quantum yield in band gap tunable bromide containing mixed halide perovskites. *Nano Lett.* **16**, 800–806 (2016).

85. Zeiske, S. et al. Sensitivity of sub-bandgap external quantum efficiency measurements of solar cells under electrical and light bias. *ACS Photon.* **7**, 256–264 (2019).

86. Cheng, Y. et al. Revealing the degradation and self-healing mechanisms in perovskite solar cells by sub-bandgap external quantum efficiency spectroscopy. *Adv. Mater.* **33**, 2006170 (2021).

87. Malliaras, G. G. et al. Electrical characteristics and efficiency of single-layer organic light-emitting diodes. *Phys. Rev. B* **58**, R13411–R13414 (1998).

88. Bube, R. H. Trap density determination by space-charge-limited currents. *J. Appl. Phys.* **33**, 1733–1737 (1962).

89. Shi, D. et al. Low trap-state density and long carrier diffusion in organolead trihalide perovskite single crystals. *Science* **347**, 519–522 (2015).

90. Saidaminov, M. I. et al. High-quality bulk hybrid perovskite single crystals within minutes by inverse temperature crystallization. *Nat. Commun.* **6**, 7586 (2015).

91. Dong, Q. et al. Electron-hole diffusion lengths > 175 μm in solution-grown CH3NH3PbI3 single crystals. *Science* **347**, 967–970 (2015).

92. Adinolfi, V. et al. The in-gap electronic state spectrum of methylammonium lead iodide single-crystal perovskites. *Adv. Mater.* **28**, 3406–3410 (2016).

93. Dong, Q. et al. Electron-hole diffusion lengths >175 μm in solution-grown CH3NH3PbI3 single crystals. *Science* **347**, 967–970 (2015).

94. Walter, T. et al. Determination of defect distributions from admittance measurements and application to Cu(In,Ga)Se2 based heterojunctions. *J. Appl. Phys.* **80**, 4411–4420 (1996).

95. Lang, D. V. Deep-level transient spectroscopy: a new method to characterize traps in semiconductors. *J. Appl. Phys.* **45**, 3023–3032 (1974).

96. Rosenberg, J. W. et al. Laplace current deep level transient spectroscopy measurements of defect states in methylammonium lead bromide single crystals. *J. Appl. Phys.* **122**, 145701 (2017).

97. Yang, W. S. et al. Iodide management in formamidinium-lead-halide–based perovskite layers for efficient solar cells. *Science* **356**, 1376–1379 (2017).

98. Haering, R. R. & Adams, E. N. Theory and application of thermally stimulated currents in photoconductors. *Phys. Rev.* **117**, 451–454 (1960).

99. Baumann, A. et al. Identification of trap states in perovskite solar cells. *J. Phys. Chem. Lett.* **6**, 2350–2354 (2015).

100. Michelson, C. E., Gelatos, A. V. & Cohen, J. D. Drive-level capacitance profiling: Its application to determining gap state densities in hydrogenated amorphous silicon films. *Appl. Phys. Lett.* **47**, 412–414 (1985).

101. Heath, J. T., Cohen, J. D. & Shafarman, W. N. Bulk and metastable defects in CuIn1−xGaxSe2 thin films using drive-level capacitance profiling. *J. Appl. Phys.* **95**, 1000–1010 (2004).

102. Duan, H.-S. et al. The role of sulfur in solution-processed Cu2ZnSn(S,Se)4 and its effect on defect properties. *Adv. Funct. Mater.* **23**, 1466–1471 (2013).

103. Tress, W. Metal halide perovskites as mixed electronic–ionic conductors: challenges and opportunities—from hysteresis to memristivity. *J. Phys. Chem. Lett.* **8**, 3106–3114 (2017).

104. Eames, C. et al. Ionic transport in hybrid lead iodide perovskite solar cells. *Nat. Commun.* **6**, 7497 (2015).

105. Jakob, D. S. et al. Integrated tapping mode Kelvin probe force microscopy with photoinduced force microscopy for correlative chemical and surface potential mapping. *Small* **17**, 2170194 (2021).

106. Kang, Z. et al. Kelvin probe force microscopy for perovskite solar cells. *Sci. China Mater.* **62**, 776–789 (2019).

107. Bergmann, V. W. et al. Real-space observation of unbalanced charge distribution inside a perovskite-sensitized solar cell. *Nat. Commun.* **5**, 5001 (2014).

108. Shao, Y. et al. Grain boundary dominated ion migration in polycrystalline organic–inorganic halide perovskite films. *Energy Environ. Sci.* **9**, 1752–1759 (2016).

109. Li, X. et al. Defect passivation effect of chemical groups on perovskite solar cells. *ACS Appl. Mater. Interfaces* **14**, 30 (2021).

110. Li, X. et al. Suppressing the ions-induced degradation for operationally stable perovskite solar cells. *Nano Energy* **64**, 103962 (2019).

111. Xing, J. et al. Ultrafast ion migration in hybrid perovskite polycrystalline thin films under light and suppression in single crystals. *Phys. Chem. Chem. Phys.* **18**, 30484–30490 (2016).

112. Liu, Y. et al. Secondary ion mass spectrometry (SIMS) for chemical characterization of metal halide perovskites. *Adv. Funct. Mater.* **30**, 2002201 (2020).

113. DeQuilettes, D. W. et al. Photo-induced halide redistribution in organic–inorganic perovskite films. *Nat. Commun.* **7**, 1–9 (2016).

114. Zhang, T. et al. Profiling the organic cation-dependent degradation of organolead halide perovskite solar cells. *J. Mater. Chem. A* **5**, 1103–1111 (2017). **Ion migration mediated degradation of perovskite solar cells as revealed from time of flight secondary ion mass spectrometry.**

115. Liu, Y. et al. Hysteretic ion migration and remanent field in metal halide perovskites. *Adv. Sci.* **7**, 2001176 (2020).

116. Gross, E. Challenges and opportunities in IR nanospectroscopy measurements of energy materials. *Nano Res.* **12**, 2200–2210 (2019).

117. Yuan, Y. et al. Photovoltaic switching mechanism in lateral structure hybrid perovskite solar cells. *Adv. Energy Mater.* **5**, 1500615 (2015).

118. Lin, Y. et al. Excess charge-carrier induced instability of hybrid perovskites. *Nat. Commun.* **9**, 4981 (2018).

119. Piatkowski, P. et al. Unraveling charge carriers generation, diffusion, and recombination in formamidinium lead triiodide perovskite polycrystalline thin film. *J. Phys. Chem. Lett.* **7**, 204–210 (2016).

120. Gao, L. et al. Potassium iodide doping strategy for high-efficiency perovskite solar cells revealed by ultrafast spectroscopy. *J. Phys. Chem. Lett.* **13**, 711–717 (2022).

121. Yan, H. et al. Ultrafast terahertz probe of photoexcited free charge carriers in organometal $CH_3NH_3PbI_3$ perovskite thin film. *Appl. Phys. A* **122**, 1–6 (2016).

122. Ulatowski, A. M. et al. Revealing ultrafast charge-carrier thermalization in tin-iodide perovskites through novel pump–push–probe terahertz spectroscopy. *ACS Photon.* **8**, 2509–2518 (2021).

123. Thiesbrummel, J. et al. Universal current losses in perovskite solar cells due to mobile ions. *Adv. Energy Mater.* **11**, 2101447 (2021).

124. Yang, W. S. et al. Iodide management in formamidinium-lead-halide–based perovskite layers for efficient solar cells. *Science* **356**, 1376–1379 (2017).

125. Hu, Y. et al. Understanding the role of cesium and rubidium additives in perovskite solar cells: trap states, charge transport, and recombination. *Adv. Energy Mater.* **8**, 1703057 (2018).

126. Liu, Y. et al. Two-inch-sized perovskite $CH_3NH_3PbX_3$ (X = Cl, Br, I) crystals: growth and characterization. *Adv. Mater.* **27**, 5176–5183 (2015).

127. Shao, Y. et al. Origin and elimination of photocurrent hysteresis by fullerene passivation in $CH_3NH_3PbI_3$ planar heterojunction solar cells. *Nat. Commun.* **5**, 5784 (2014).

128. Lin, Y. et al. Matching charge extraction contact for wide-bandgap perovskite solar cells. *Adv. Mater.* **29**, 1700607 (2017).

129. Lin, Y. et al. π-Conjugated Lewis base: efficient trap-passivation and charge-extraction for hybrid perovskite solar cells. *Adv. Mater.* **29**, 1604545 (2017).

130. Ho, K. et al. Grain transformation and degradation mechanism of formamidinium and cesium lead iodide perovskite under humidity and light. *ACS Energy Lett.* **6**, 934–940 (2021).

131. Ni, Z. et al. Evolution of defects during the degradation of metal halide perovskite solar cells under reverse bias and illumination. *Nat. Energy* **7**, 65–73 (2022).

132. Lin, Y. et al. Excess charge-carrier induced instability of hybrid perovskites. *Nat. Commun.* **9**, 1–9 (2018).

Acknowledgements

Author contributions

S.S., S.R., L.Y., and D.A.: Conceptualization, investigation, roles/writing—original draft; T.S. and S.C.: Investigation, roles/writing—original draft; A.S., S.S., and R.K.G.: Funding acquisition, resources, supervision; roles/writing—review & editing; A.G.: Funding acquisition, resources, supervision, roles/ writing—review & editing; K.S.N.: Conceptualization, investigation, funding acquisition, resources, supervision, roles/writing—review & editing.

Competing interests

The authors declare no competing interests.

Additional information

Correspondence and requests for materials should be addressed to Anand Singh, Raju Kumar Gupta, Ashish Garg or Kanwar S. Nalwa.

Peer review information *Communications Materials* thanks the anonymous reviewers for their contribution to the peer review of this work. Primary Handling Editors: Jet-Sing Lee and John Plummer.

Reprints and permission information is available at http://www.nature.com/reprints

Publisher's note Springer Nature remains neutral with regard to jurisdictional claims in published maps and institutional affiliations.